



# Palaeontological and sedimentological studies of dated cores from the coast of Thyna (Sfax, Gulf of Gabes, Tunisia): multiproxy evidence for a high-energy extreme event and palaeoenvironmental reconstructions

Mohamed Kamoun<sup>1</sup> · Chahira Zaïbi<sup>1</sup> · Khawla Ben Khalifa<sup>1</sup> · Maria da Conceição Freitas<sup>2,6</sup> · Martin R. Langer<sup>3</sup> · Ana Maria Costa<sup>2,4,5</sup> · Pedro J. M. Costa<sup>2,7</sup> · César Andrade<sup>2,6</sup> · Skye Yunshu Tian<sup>3</sup> · Najib Bahrouni<sup>8</sup> · Fekri Kamoun<sup>1</sup>

Received: 13 October 2023 / Accepted: 20 February 2024  
© Springer Nature Switzerland AG 2024

## Abstract

In this paper, sedimentological, geochemical, palaeontological and radiocarbon dating results from Holocene cores are presented to infer the palaeoenvironmental evolution of the Thyna coast in the Gulf of Gabes (Tunisia). Based on detailed faunal, sedimentological and geochemical analyses, the evolution of the coastline and the impact of a high-energy event around 365 CE which led to the destruction of parts of the historic city of Thyna are reconstructed. The scenario developed here is based on the analysis of four drill cores and shows an evolution from a shallow marine palaeoenvironment to a gradually enclosed lagoon. The core record includes the following. (i) Evidence of the first Holocene transgression at around 6234–5733 cal year BCE (8184–7683 cal yr BP), characterised by the first appearance of foraminifera and molluscs. The transgressive sediments of the first transgression overlie the Upper Pleistocene–Greenlandian terrigenous clays. (ii) Deposits of a high-energy event that formed in the fourth century after the Crete earthquake (365 AD). The bioclastic deposits are characterised by an erosive base and are rich in rip-up clasts, charcoal particles, wood and pottery fragments, and abundant shell debris. This deposit comprises a blend of remains from coastal and lagoonal molluscs, along with brackish foraminifera originating from the more internal regions of a confined lagoon. (iii) After the high-energy event, there is evidence of a partially open lagoon off the coast, which was protected from the open sea by a sand barrier. (iv) Evidence of increased marine influence and further opening of the lagoon in the nineteenth and twentieth centuries, suggesting that the coastal area of Thyna is affected not only by the current sea level rise but probably also by subsidence. The scenario developed and the events identified here are compared with those already known.

**Keywords** Foraminifera · Sedimentary facies · Molluscs · Geochemistry

---

Responsible Editor: João Miguel Dias.

---

✉ Mohamed Kamoun  
med23km@yahoo.fr

<sup>1</sup> GEOGLOB Laboratory, Faculty of Sciences of Sfax, Sfax University, BP 1171, 3000 Sfax, Tunisia

<sup>2</sup> Instituto Dom Luiz (IDL), Universidade de Lisboa, Campo Grande, 1749-016 Lisbon, Portugal

<sup>3</sup> Institut für Geowissenschaften Paläontologie, Universität Bonn, Nussallee 8, 53115 Bonn, Germany

<sup>4</sup> Laboratório de Arqueociências (LARC)-DGPC, Calçada do Mirante à Ajuda, No 10A, 1300-418 Lisbon, Portugal

<sup>5</sup> BIOPOLIS and CIBIO, Research Centre in Biodiversity and Genetic Resources, University of Porto, Porto, Portugal

<sup>6</sup> Departamento de Geologia, Faculdade de Ciências, Universidade de Lisboa, Campo Grande, 1749-016 Lisbon, Portugal

<sup>7</sup> Departamento de Ciências da Terra, Faculdade de Ciências e Tecnologia, Universidade de Coimbra, Rua Sílvio Lima, Univ. Coimbra-Polo II, 3030-790 Coimbra, Portugal

<sup>8</sup> Geological Service, National Office of Mines, 24, Street of Energy, 2035 Chargaia, Tunis, Tunisia

## Introduction

In recent decades, research on global change and extreme events, as well as on how they manifest themselves in the geological record, has increased exponentially (Freitas et al. 2002; Kortekaas et al. 2003; Kortekass 2022; Vigliotti et al. 2019; Putra et al. 2019). In Tunisia, coastal wetlands are under severe anthropogenic stress due to, for example, increasing freshwater scarcity, salinisation (El Kateb et al. 2018) and pollution (Damak et al. 2019; Gargouri et al. 2015). These vulnerable areas have been impacted by both global change and human activities, as reflected in warming ocean waters, rising sea levels, extreme events and changes in the sediment dynamics (Bahrouni et al. 2021; Khadraoui et al. 2018; Kohila et al. 2021; Ameur et al. 2021). The main objectives of this work are to identify environmental and landscape changes recorded in sediments along the Thyna coast in recent millennia and to characterise the impact of high-energy marine events. High-energy events can be recognised through the analysis of palaeontological and sedimentological data in core records, and markers of palaeoenvironmental changes in coastal sediments have been identified as indicators of high-energy events and tracers of tsunami. Examples include (i) mollusc associations and their taphonomic characteristics (Bony et al. 2012; Khadraoui et al. 2018; Kitamura et al. 2018; Puga-Bernabéu and Aguirre 2017); (ii) mixtures of diatom associations from different sources and their degrees of preservation (Dura and Hemphill-Haley 2020); and (iii) the preservation of ostracod carapaces and the structure of the population (Husain et al. 2010; Kamoun et al. 2021; Ruiz et al. 2010). In addition, foraminifera have played a crucial role as proxies when reconstructing high-energy events and tsunamis (e.g. Fischer et al. 2016; Hawkes 2020; Mamo et al. 2009; Putra et al. 2022; Quintela et al. 2016). The recognition of the peculiarities of the foraminiferal assemblages and of the taphonomy of the tests in the coastal sediments makes it possible to recognise the tsunami deposits and to distinguish them from the storm deposits as long as this is combined with a facies interpretation (e.g. Kortekaas 2002, Nagendra et al. 2005; Kortekaas and Dawson 2007; Dawson 2007; Dawson and Shi 2000; Hawkes et al. 2007; Pilarczyk et al. 2014, 2020). Sedimentological criteria such as the presence of large boulders and sharp basal and upper contacts also distinguish the high-energy deposits from regular sediment sequences (Goff and Chagué-Goff 2015; Judd et al. 2017; Vigliotti et al. 2019; Puga-Bernabéu and Aguirre 2017; Putra et al. 2019, 2022). Bony et al. (2012), Fischer et al. (2016) and Morton et al. (2008) consider the interstratification of coarse sediments in layers of finer sediments, fining-upward and thinning-landward

sequences, and the presence of rip-up clasts as sedimentological features that can be used to identify tsunami deposits. In addition, several authors discuss the extent and elevation of land-based deposits as possible key factors in the distinction between tsunami and storm deposits (Chagué-Goff et al. 2012; Dawson 1994; Jaffe et al. 2012; Kortekaas and Dawson 2007; Morton et al. 2007; Szczuciński et al. 2012). De Martini et al. (2020), based on data from 66 Mediterranean coastal sites, conclude that “tsunami deposits are characterized by a predominance of fine sediment layers (68%), followed by transported blocks (25%) and geomorphological signatures (7%); 11% of sites exceeds the value of 10 m in elevation a.s.l. (above sea level), while the inundation distance of 17% of the sites overcomes 500 m inland”. The documentation of high-energy/tsunami events is also possible by means of geochemical sediment proxies, in particular high concentration values of marine elements such as Ca, Cl, Sr and Ti (Judd et al. 2017; Moreira et al. 2017) and terrigenous elements (Zr, Fe, Ti, Al, Si, K, and Fe/Ti; Chagué-Goff et al. 2002; Wedepohl 1971). Tsunami deposits have been identified and described from both prehistoric and historical coastal sedimentary sequences in Italy (Mastronuzzi and Sansò 2004), Spain (Kelletat et al. 2005), Morocco (Basquin et al. 2023) and along the eastern Mediterranean coasts (Greece: Scheffers and Scheffers 2007; Cyprus: Kelletat and Schellmann 2002; and the Hellenic zone: Salama et al. 2018).

Along the southern Mediterranean coast, Papadopoulos (2009) compiled historical data on tsunamis that affected the Algerian coast in 1365, 1773, 1856, 1954 and 1980 CE. Along the Alexandria coastline (Egypt), multiproxy analyses of sediments in trenches and cores show correlations with tsunamigenic earthquakes in 1600 BC and in 365 and 1303 AD as well as the 1870 AD Hellenic zone event (Salama et al. 2018). Based on geophysical surveys and sediment core analysis from the Ionian Sea, Polonia et al. (2013) showed that the 20- to 25-m-thick megaturbidite was triggered by the 365 CE Cretan earthquake and tsunami. In the *Catalogue of Ancient Earthquakes for the Mediterranean*, Ammianus Marcellinus (in Guidoboni et al. 1994) described the devastating effects of a tsunami that struck Antioch (Turkey) in 365 AD as follows: “the sea was driven back and its waters flowed away flattened many buildings in the towns or wherever they were encountered”.

On the Tunisian coast at Haouaria (Cap Bon, northern Tunisia), May et al. (2010) described an imbricated boulder accumulation that had been transported 50 m inland and suggested a correlation with an undated tsunami event (Fig. 1A). At Nabeul (Neapolis), archaeological work suggests the occurrence of a catastrophic inundation event following a landslide in the fourth century AD (Fantar et al. 2019). Kohila et al. (2021) identified two marine inundation

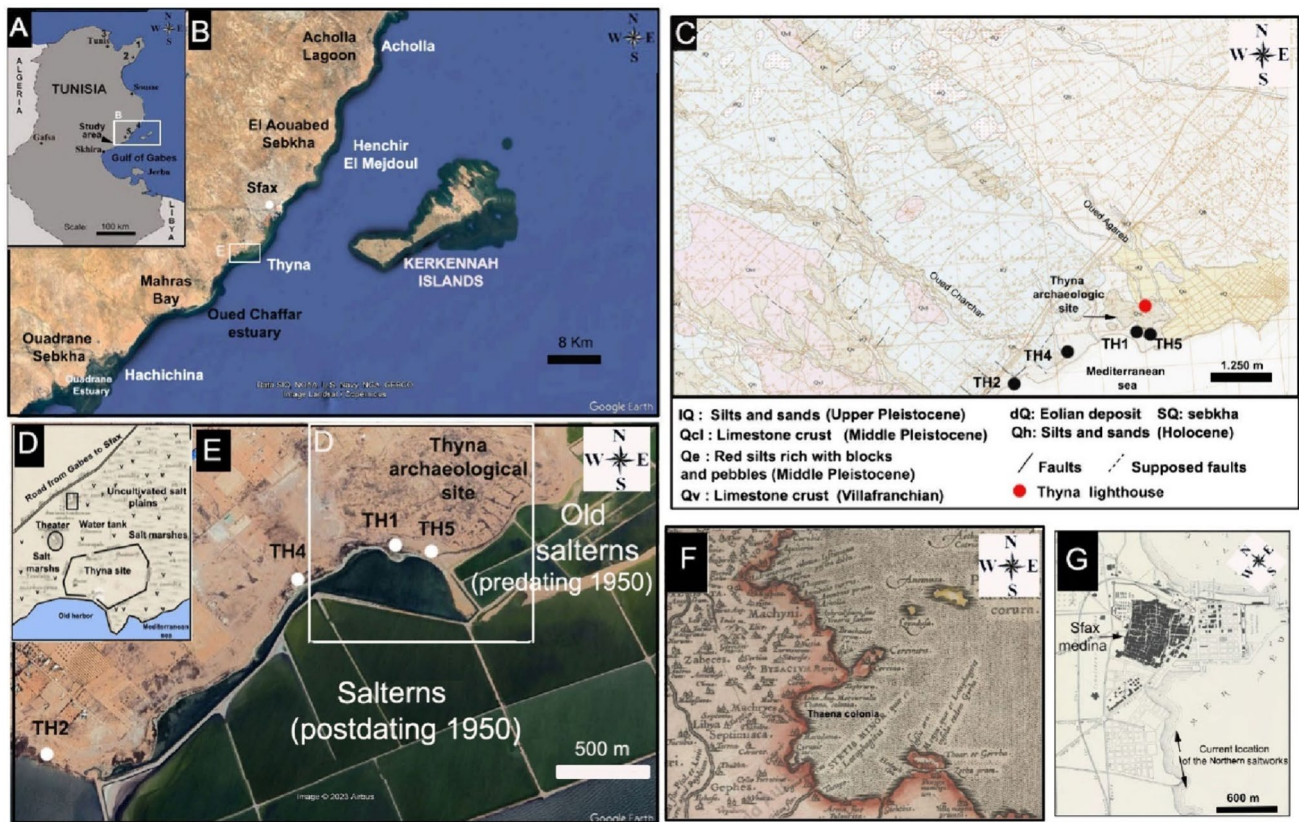


**Fig. 1** **A** Location of the study area and the sites described in the main text on maps of Tunisia: 1 Haouaria, 2 Nabeul (Neapolis), 3 Ghar El Melh, 4 Acholla, 5 Henchir El Mejdoul. **B** Map of the coastal area between Acholla and Hachichina, showing bays, lagoons, sebkhas and the Ouadrane Estuary (source: Google Earth, mission 2023/04/15). **C** Geologic map of Thyna and the adjacent area (after Bouaziz et al. 2004, Agareb map). **D** Historic map (1888) of the Thyna coast, showing the location of the harbour and the salt marsh around the historic city of Thyna (after Servonnet and Lafitte

1888). **E** Main geographical features of the Sfax coast, location of the study area and locations of cores (source: Google Earth, mission 2023/04/15). **F** Historic map (dated to approx. 1590 AD) of the eastern Tunisian coast between Menyx, Jerba, Hadrumetum and Sousse, showing Thaena Colonia and the Thyna archaeological site (after Gastaldi and Licinus 1564). **G** Historic map (dating from 1900 AD) of the northern coast near the city of Sfax, revealing the absence of saltworks (Picard 1900)

events in the Ghar El Melah lagoon (northern Tunisia) using sedimentological analyses applied to sediment cores dated by isotopic techniques. The first event seems to coincide with the 365 AD tsunami, while the second could be related to the 1693 AD tsunami in southern Italy or to an increase in extreme storm events.

Frébourg et al. (2010) suggest the possibility of an 8-ka-BP tsunami deposit within the outcrop of the Sidi Salem Eolianite Formation on the coast of Djerba Island (southern Tunisia), based on sedimentological analysis and the palaeo-altitude of the outcrop.

A tsunami deposit dated to 1448–1950 cal BP has been described by Khadraoui et al. (2018) along the coast north of Sfax and at Henchir El Mejdoul (Fig. 1B). Recent field investigations have re-dated this event to around 365 AD. This is based on radiocarbon dating of charcoal samples collected above and below the catastrophic units (Bahrouni et al. 2021). At the Hachichina coast (Fig. 1B), this

event may be responsible for overtopping sand spits and transporting marine coarse sands hosting a mix of brackish and marine macro- and microfauna further inland (Ben Khalifa et al. 2019).

Examination of sediment units in cores collected from the Acholla coast, 50 km north of Sfax (Fig. 1B), revealed changes in ostracod and mollusc assemblages and population structures, with only juveniles or adults of different species present, suggesting displacement and redeposition by a high-energy event, possibly a tsunami, around 417 CE, according to Kamoun et al. (2021). Given that this date was obtained from sediment 10 cm above the top of the event layer, a source related to the 365 CE Crete tsunami cannot be ruled out.

In this study, we examine the sedimentary facies, the geochemical characteristics of the sediments, and the mollusc and foraminiferal records of sediment cores collected along the coast of Thyna (Fig. 1E).

The main objectives are (i) to reveal the Holocene palaeoenvironmental evolution of the Thyna coast, (ii) to identify the signatures of marine transgressions and extreme marine events recorded in the sediments of this area, (iii) to determine the anthropogenic impact on the coastal landscape and environmental change, and (iv) to investigate whether the 365 AD Crete earthquake/tsunami is recorded in the Roman ruins of Thyna and along the surrounding coastal geological record. The information is supplemented by historical data as well. We also describe the importance of the palaeontologic, sedimentologic and geochemical records in identifying these events. The study is framed by recent research on both tsunami events in the Mediterranean basin and state-of-the-art palaeoenvironmental investigations of the Tunisian coast.

### The study region of Thyna

The coast of Thyna is part of the Sfax region (Fig. 1A, B), which occupies a lowland area partly composed of wetlands. The wetlands are affected by active subsidence and show several signs of erosion and salinisation (Oueslati 2021; Slim et al. 2004). The average altitude is less than 2 m above sea level, and the area includes sebkhas, slikkes and schorres, which are subject to the influence of sea water. The sebkhas and schorres are constantly waterlogged and are often flooded after rain or sea storms or by rising groundwater. The climate is warm and dry, with an average rainfall of only about 150 mm/year and an average annual temperature of 18.9 °C.

### Geomorphology

The coastal environment of Thyna (Fig. 1E) experiences a semi-diurnal tidal range of 140 cm during spring tides to 30 cm during neap tides (Amari 1984). It can be divided into several zones: (1) a supratidal zone (in front of the archaeological site) that is inundated during exceptional floods, composed of sebkhas to the west and reveals a muddy sand substrate rich in microbial mats; (2) an extensive intertidal zone composed of sandy silt, devoid of vegetation (slikkes) and dominated by dense stands of salt-tolerant plants in the upper zone (salt marshes covered by dense *Salicornia* meadows and dense reeds); and (3) a subtidal zone, permanently flooded, which is characterised by silt and *Posidonia* and *Cymodocea* seagrass. A peculiarity of the coast of Thyna is the presence of salterns along the seashore. They extend over 12 km of coastline and cover an area of around 1700 ha (Fig. 1E). The salterns were probably built after 1900 AD between the port of Sfax and Thyna and occupy the former intertidal zone about 1 m below mean sea level (Fig. 1E). This is indicated by nautical charts from 1590 AD, 1888 AD

and 1900 AD (Fig. 1D, F, G; see also Brogan and Kenyon 1966).

### Geological setting

The Thyna hinterland is included in the Agareb geological map (Bouaziz et al. 2004) and is characterised by a series of NW–SE- and NE–SW-trending faults (Fig. 1C). Mio-Pliocene outcrops are rare and represented by reddish gypsum clays, which do not occur in the study area. Most of the region is therefore Quaternary (including recent deposits). The oldest are the Villafranchian limestone crusts, which generally consist of two levels: a powdery crust at the base and a hardground rich in helioid snails at the top. The Villafranchian crust (Qv) is covered by (i) red silt with calcareous concretions and large reworked blocks and cobbles (Villafranchian, Middle Pleistocene; Qe) and (ii) red silt and sand (continental Upper Pleistocene; IQ). The Upper Pleistocene marine sandy facies rich in *Cerithium vulgatum*, *Persististrombus latus* and *Cerastoderma glaucum* (correlated with the marine isotopic stage, MIS, 5e), which outcrops north of Sfax, is absent from the Thyna coast. The Holocene sediments (Qh) consist mainly of silt and sand (Ghribi et al. 2006).

### Archaeological data

The historic site of Thyna was built on a promontory 12 km south of Sfax (Fig. 1D, E). An ancient Punic city, it came under Numidian rule after the fall of Carthage in 146 BC and became Roman in 46 BC (Slim et al. 2004). The port of Thyna must have existed in ancient times (Fendri 1985). The map of the Thyna region drawn in 1888 AD by Servonnet and Lafitte (1888) shows that the archaeological site was surrounded by salt marshes in its western part and uncultivated salt plains in its eastern part, and the ancient harbour was located in front of the southern ramparts of the city (Fig. 1D). These authors reported that “Thyna had an elliptical harbour basin three-quarters filled with sand, but serial photographs and local investigations showed no sign of this”. The city of Thyna was occupied for a long period until it was abandoned in the mid-seventh century AD following the Arab conquests (Fendri 1985). The Arabs borrowed many of the buildings that were in ruins, and the Roman city became a veritable stone quarry.

### Materials and methods

Five sediment cores were drilled in the supratidal zone along the Thyna coast (TH1/TH1B, TH2, TH4 and TH5; Fig. 1C–E). TH1, TH2 and TH4 were retrieved in April 2021, and TH5 and TH1B (a replicate of TH1) were drilled in June

2022. Cores were obtained by inserting a 60-mm-diameter PVC pipe by hammering. The compaction ratio can be calculated by comparing the length of the extracted core sediment with the length of the inserted PVC tube. The ratio was on the order of 0.66 and was used to calculate the real length of the core sediment. In the laboratory, the cores were split lengthwise and photographed. Facies were classified based on their lithology, granulometry, and mollusc and foraminifera associations.

The TH1B and TH5 sediments were analysed to determine their magnetic susceptibility, texture, and organic matter and calcium carbonate contents. The volume magnetic susceptibility (MS) was directly measured in SI units on the core using a Bartington® MS2 instrument equipped with an MS2E surface scanner. Grain size was determined by wet sieving using a 63- $\mu\text{m}$  mesh sieve, and the sediment was classified according to Flemming (2000). The coarse fraction ( $> 63 \mu\text{m}$ ) was then sieved using a normalised series of ASTM sieves between  $4 \phi$  (63  $\mu\text{m}$ ) and  $-2 \phi$  (4 mm) at  $0.5\text{-}\phi$  intervals. Statistical values for the grain size distribution were determined using the GRADISTAT software (Blott and Kenneth 2000) and were then used to categorise the samples according to the method of Folk and Ward (1957). Organic matter (% OM) content was determined by loss on ignition (LOI) using 0.5 g of ground sediment heated in a muffle furnace at 520 °C for 6 h. Calcium carbonate (%  $\text{CaCO}_3$ ) content was determined using an Eijkelkamp calcimeter that measures the  $\text{CO}_2$  produced by the reaction of calcium carbonate with HCl (4 mol/L) in a sample of known mass.

Molluscs and foraminifera were identified in cores TH1, TH2 and TH4. For species identifications, we used the reference catalogues of Bouchet and Rocroi (2010) for molluscs and a catalogue of Mediterranean foraminifera (Cimerman and Langer 1991) along with additional literature (Langer 1988, 1993; Langer and Schmidt-Sinns 2006; Trog et al. 2013; Fajemila et al. 2015). All identifications were cross-checked with the World Register of Marine Species (WoRMS, <https://www.marinespecies.org>; Table 1, Fig. 2). Selected samples were wet sieved using 63-, 125-, 250- and 500- $\mu\text{m}$  mesh sieves. Levels were sampled at 14-cm intervals, and a higher resolution was used for selected facies intervals. All molluscs and foraminifera were picked from the 125- and 250- $\mu\text{m}$  fractions of the core samples, and the total number of individuals was counted for each species. Diversity indices, including the equitability ( $E$ ), Shannon ( $H$ ) and dominance ( $D$ ) indices, were calculated using the software package PAST V 2.04 (Hammer et al. 2001). To investigate faunal transitions throughout the core, we used  $k$ -means cluster analysis and the elbow method for statistical analysis (Hartigan and Wong 1979).

Benthic foraminifera were divided into five groups based on their substrate, salinity and microhabitat

preferences (Langer 1993; Trog et al. 2013; Cimerman and Langer 1991) to infer changes in the environmental setting, including substrate characteristics and the variation of salinity over time (Langer 1993; Trog et al. 2013; Cimerman and Langer 1991): *group I* contains ammoniid foraminifera—indicators of stressful environmental conditions in shallow waters of the intertidal zone; *group II* comprises elphidiids—indicators of shallow littoral environments; *group III* contains miliolids, which characterise shallow coastal habitats; *group IV* includes symbiont-bearing peneroplids—indicators of well-oxygenated environments with seagrasses (*Posidonia oceanica*) and algae; and *group V* comprises rosalinid foraminifera—indicators of algae or other hard substrates.

R-mode cluster analysis was performed using the paired-group algorithm and the Bray–Curtis similarity index on the raw data of major foraminifera species that were standardised to  $> 2\%$  via constant weight. The results of the cluster analysis allowed us to identify assemblages, recognise ecological affinities between species and infer environmental conditions. In addition, a correspondence analysis (CA) was performed based on the absolute abundance of foraminifera by using PAST software to verify the interpretation. For this, we selected core TH1, as it provides the most robust data set.

A total of 50 samples from cores TH1, TH2 and TH5 were selected for geochemical analysis at the Mineralogy Laboratory (Faculty of Sciences, Sfax). The concentrations of 14 elements (Fe, Mn, V, Zr, Ti, Si, Mg, Rb, K, Cl, S, Ca, Sr and Al) in powdered material were determined using a Niton FXL X-ray fluorescence (XRF) analyser (Thermo Scientific). The concentrations of the major elements were normalised to Al (Martinez-Ruiz et al. 2015). The element ratios K/Al, Mg/Al, and Rb/Al can be used to infer possible terrigenous input, while the high values of Si/Al, Ti/Al and Zr/Al might characterise aeolian input (Calvert and Pedersen 2007; Govin et al. 2012). The marine influence can be recognised from the high values of Ca/Al, Cl/Al and Sr/Al (Martinez-Ruiz et al. 2015; Judd et al. 2017).

Nine samples were radiocarbon dated ( $^{14}\text{C}$ ) at the Institute of Geology and Mineralogy at the University of Cologne, Germany. Charcoal, plant/wood and bulk organic matter samples were selected for dating (Table 2). The samples were prepared following Rethemeyer et al. (2019). Conventional ages were calibrated with OxCal v. 4.4.4 (© Bronk Ramsey, 2021) using the calibration curve IntCal20 (Reimer et al. 2020) for terrestrial materials (from cores TH1 and TH2) and the Marine20 (Heaton et al. 2020) calibration curve for marine organic materials (for core TH5). The results are expressed in BCE/CE.

**Table 1** Foraminifera and mollusc taxa recorded in sediment samples from cores TH1, TH2 and TH4**Foraminifera**

<i>Adelosina</i> sp.	<i>Nonion</i> sp.
<i>Agglutinella</i> sp.	<i>Nonionella</i> sp.
<i>Ammonia parkinsoniana</i> (d'Orbigny, 1839)	<i>Nubecularia lucifuga</i> Defrance, 1825
<i>Ammonia</i> sp. 1	<i>Peneroplis planatus</i> (Fichtel & Moll, 1798)
<i>Ammonia</i> sp. 2	<i>Planulina</i> sp.
<i>Ammonia aberdoveyensis</i> Haynes, 1973	<i>Quinqueloculina pseudobuchiana</i> Łuczowska, 1974?
<i>Ammonia veneta</i> (Schultze, 1854)	<i>Quinqueloculina seminulum</i> (Linnaeus, 1758)
<i>Buccella</i> sp.	<i>Quinqueloculina</i> sp.
<i>Epistominella naraensis</i> (Kuwano, 1950)	<i>Quinqueloculina striata</i> d'Orbigny in Guérin-Méneville, 1832
<i>Cibicides pachyderma</i> (Rzehak, 1886)	<i>Quinqueloculina</i> cf. <i>Quinqueloculina vulgaris</i> d'Orbigny, 1826
<i>Cibicides</i> sp.	<i>Rosalina floridana</i> ? (Cushman, 1922)
<i>Cymbaloporella bradyi</i> (Cushman, 1915)	<i>Rosalina bradyi</i> (Cushman, 1915)
<i>Cymbaloporella squamosa</i> (d'Orbigny, 1839)	<i>Rosalina globularis</i> d'Orbigny, 1826
<i>Discorbinella bertheloti</i> (d'Orbigny, 1839)	<i>Rosalina macropora</i> (Hofker, 1951)
<i>Discorbinella subcomplanata</i> (Parr, 1950)	<i>Rosalina</i> sp. 1
<i>Elphidium aculeatum</i> (d'Orbigny, 1846)	<i>Rosalina williamsoni</i> (Chapman & Parr, 1932)
<i>Elphidium advenum</i> (Cushman, 1922)	<i>Rotorbis auberii</i> (d'Orbigny, 1839)
<i>Elphidium excavatum</i> (Terquem, 1875)	<i>Quinqueloculina agglutinans</i> d'Orbigny, 1839
<i>Elphidium fichtelianum</i> (d'Orbigny, 1846)	<i>Siphonaperta dilatata</i> (Le Calvez & Le Calvez, 1958)
<i>Elphidium macellum</i> (Fichtel & Moll, 1798)	<i>Siphonina</i> sp.
<i>Elphidium sagra</i> (d'Orbigny, 1839)	<i>Spiroloculina</i> sp. 1
<i>Hauerina</i> sp.	<i>Triloculina</i> sp. 2
<i>Haynesina depressula</i> (Walker & Jacob, 1798)	<i>Triloculina trihedra</i> Loeblich & Tappan, 1953
<i>Haynesina germanica</i> (Ehrenberg, 1840)	<i>Trochammina inflata</i> (Montagu, 1808)
<i>Haynesina</i> sp.	<i>Valvulineria</i> sp.
<i>Massilina</i> sp.	<i>Vertebralina striata</i> d'Orbigny, 1826
<i>Melonis</i> sp.	
<i>Triloculinella dilatata</i> (d'Orbigny, 1839)	
<i>Neoconorbina</i> sp. 1	

**Molluscs**

<i>Abra alba</i> (W. Wood, 1802)	<i>Loripes orbiculatus</i> Poli, 1795
<i>Bittium reticulatum</i> (da Costa, 1778)	<i>Natica</i> sp.
<i>Bulla striata</i> Bruguière, 1792	<i>Neverita josephina</i> Risso, 1826
<i>Cerastoderma glaucum</i> (Bruguière, 1789)	<i>Nassarius sufflatus</i> (A. Gould, 1860)
<i>Cerithium vulgatum</i> Bruguière, 1792	<i>Nassarius mutabilis</i> (Linnaeus, 1758)
<i>Dentalium dentalis</i> = <i>Antalis dentalis</i> Linnaeus, 1758	<i>Pirenella conica</i> (Blainville, 1929)
<i>Dendropoma</i> sp.	<i>Rissoa</i> sp.
<i>Epitonium</i> sp.	<i>Retusa desgenettii</i> (Audouin, 1826)
<i>Gibbula umbicularis</i> = <i>Steromphala umbilicaris</i> (Linnaeus, 1758)	<i>Ruditapes decussatus</i> (Linnaeus, 1758)
<i>Hexaplex trunculus</i> (Linnaeus, 1758)	<i>Scaphander</i> sp.
<i>Ecrobia truncata ventrosa</i> (Montagu, 1803)	<i>Turritella comminus</i> = <i>Turritellinella tricarinata</i> (Brocchi, 1814)
<i>Ecrobia truncata</i> (Vanatta, 1924) = <i>Hydrobia truncata</i>	<i>Turbonilla acuta</i> (Donovan, 1804)
<i>Cerithium vulgatum</i> Bruguière, 1792	

## Results

### Dating

The chronology of the events recorded in Thyna sediments was compiled by using the nine radiocarbon dates obtained from different cores (Table 2). Based on the obtained dates, it can be concluded that the sedimentary sequence of Thyna was deposited over the last 8000 years, covering the Northgrippian and Meghalayan stages.

All dates were calibrated using Oxcal v.4.4.4 (© Bronk Ramsey). TH1 and TH2 dates produced on charcoal and macro-plant remains from terrestrial environments were calibrated using the IntCal20 curve. TH5 dates were produced on marine organic materials and calibrated using the Marine20 calibration curve (Heaton et al. 2020). The ages are expressed in BCE/CE. Median values are reported.

### Sedimentary facies and molluscs

#### TH1 and TH1B cores

Core TH1 has a total length of 340 cm. The TH1B replicate core is longer, reaching 400 cm. These cores comprise 11 sedimentary facies types, as indicated by their malacological contents and textural and compositional properties (Figs. 3, 4, 5, 6).

*Facies a (Fa)*: the interval 340–325 cm (corresponding to 400–376 cm in TH1B) below surface (dbs) is made up of azoic, yellow-to-reddish sandy mud with high values of MS ( $6\text{--}22 \times 10^{-5}$  SI) and corresponds to the bedrock, which is probably Upper Pleistocene in age. Only one sample from TH1B was analysed for  $\text{CaCO}_3$  (12%) and OM (3%) contents. Both values are high and correspond to calcite precipitates and an overrated estimation of OM. The latter is most likely attributable to either the loss of water associated with the high clay content (Mook and Hoskin 1982; Dankers and Laane 1983; Barill-Boyer et al. 2003), the presence of Fe hydroxides (consistent with the sediment colour) that dehydrate at the temperatures that were used to burn OM in the furnace (e.g. Strezov et al. 2010; Beuria et al. 2017; Dweck 2008), or both. The bedrock is also marked by low levels of marine (Cl/Al, S/Al, Ca/Al and Sr/Al) and aeolian (Zr/Al, Si/Al and Ti/Al) elements.

*Facies b (Fb)*: the interval 325–295 cm dbs (376–360 cm dbs in TH1B) consists of grey/yellow muddy fine sand and is characterised by the first appearance of marine and brackish molluscs. The content of  $\text{CaCO}_3$  (shell fragments and small gastropods) varies between 7% and 9%. The MS is low (essentially between 1 and  $4 \times 10^{-5}$  SI), and the OM content is also low (around 1%).

*Facies c (Fc)*: the interval 295–265 cm dbs (360–295 cm dbs in TH1B), dated to post 6234–5733 BCE, presents a grey muddy sand rich in numerous *Posidonia* debris levels (OM is around 1.5%). Coastal molluscs are dominant (up to 70%) and lagoonal molluscs do not exceed 40%. The  $\text{CaCO}_3$  values range from 8% to 13%, while the MS remains low, typically ranging between 0 and  $6 \times 6 \times 10^{-5}$  SI. This facies exhibits the highest values for marine and detrital elemental ratios.

*Facies d (Fd)*: the interval 265–235 cm dbs (295–270 cm dbs in TH1B) consists of grey, slightly muddy sands that can be distinguished from the underlying facies by the richness in coarse materials, which make up 15% of the total sediment and consist essentially of bioclasts. OM is around 1%,  $\text{CaCO}_3$  is around 8% and MS is low (essentially between 2 and  $3 \times 10^{-5}$  SI). Lagoonal molluscs constitute up to 60%, and coastal gastropod taxa do not exceed 40%. In this facies, we recorded a decrease in the Fe/Al and Mn/Al elemental ratios.

*Facies e (Fe)*: the interval 235–140 cm dbs (270–210 cm dbs in TH1B), which covers the time interval from 3140–2890 BC (at 181–183 cm depth) to 2786–2452 BC (at 145–147 cm depth) (Table 1), consists of grey, slightly muddy sand and is rich in lagoonal molluscs (70% of the macrofossils) and associated coastal taxa.  $\text{CaCO}_3$  varies between 7% and 10% and is related to the presence of shells and shell fragments of bivalves and gastropods. OM varies between 1.2% and 1.6%, reflecting the presence of *Posidonia* seagrass. MS is zero. Fe and marine elemental ratios (Sr/Al, Ca/Al, Cl/Al and S/Al) show a strong decline.

*Facies f (Ff)*: the interval 140–118 cm dbs (210–170 cm dbs in TH1B) consists of slightly muddy sand, with the coarse fraction ( $> 0.5$  mm) reaching up to 30% of the total sediment. The basal contact of Ff is marked by a sharp erosional surface overlain by irregular rip-up lithoclasts (Fig. 7B, Ff) that probably originated from Lower Pleistocene (Villafranchian) outcrops located inland (Fig. 5). Lagoonal molluscs are dominant (90%) and show the highest individual numbers (75 ind./gr) among all the samples.  $\text{CaCO}_3$  is consistently around 6–7%, which is related to the presence of shell fragments and whole shells of bivalves and gastropods. OM varies between 1.5% and 2% and reflects the presence of *Posidonia*. MS remains at zero.

*Facies g (Fg)*: the interval 118–102 cm dbs (170–120 cm dbs in TH1B) consists of slightly muddy sand with bioclasts. The  $\text{CaCO}_3$  content varies between 5% and 8%, and OM varies between 1.7% and 2%. MS remains at zero. The individual number of molluscs does not exceed 13 ind./gr, and coastal molluscs are reduced.

*Facies h (Fh)*: the interval 102–78 cm dbs (120–90 cm dbs in TH1B) is marked by an increase in coarse materials ( $> 500$   $\mu\text{m}$ ), which reach up to 60% of the total sediment,



- 1-2. *Neverita josephinia* Risso, 1826 (x1)  
 3. *Pirenella conica* (Blainville, 1829) (x3)  
 4. *Hexaplex trunculus*, (Linnaeus, 1758) (x1)  
 5. *Retusa desgenettii* (Audouin, 1826) (x3)  
 6-7. *Nassarius sufflatus* (A. Gould, 1860) (x1,5)  
 8. *Columbella rustica* (Linnaeus, 1758) (x1,5)  
 9. *Nassarius mutabilis* (Linnaeus, 1758) (x1,5)  
 10. *Cerithium vulgatum* Bruguière, 1792 (x1)  
 11. *Comus ventricosus* Gmelin, 1791 (x1/5)  
 12. *Loripes orbiculatus* Poli, 1795 (x1)  
 13. *Bulla striata* Bruguière, 1792 (x3)  
 14. *Cerithium* sp. (x1)  
 15. *Ruditapes decussatus* (Linnaeus, 1758) (x1)  
 16. *Cerastoderma glaucum* (Bruguière, 1789)  
 17. *Ecrobia ventrosa* (Montagu, 1803) (x2)  
 18. *Abra alba* (W. Wood, 1802) (x7)  
 19-20. *Denropoma* sp. (x2)  
 21. *Dentalium dentalis* Linnaeus, 1758 (x2)  
 22. *Bittium reticulatum* (da Costa, 1778) (x1,5)  
 23. *Turbonilla acuta* (Donovan, 1804) (x2)



◀**Fig. 2** 1–2. *Neverita josephina* Risso, 1826 (×1). 3. *Pirenella conica* (Blainville, 1829) (×3). 4. *Hexaplex trunculus*, (Linnaeus, 1758) (×1). 5. *Retusa desgenettii* (Audouin, 1826) (×3). 6–7. *Nassarius sufflatus* (A. Gould, 1860) (×1.5). 8. *Columbella rustica* (Linnaeus, 1758) (×1.5). 9. *Nassarius mutabilis* (Linnaeus, 1758) (×1.5). 10. *Cerithium vulgatum* Bruguière, 1792 (×1). 11. *Conus ventricosus* Gmelin, 1791 (×1/5). 12. *Loripes orbiculatus* Poli, 1795 (×1). 13. *Bulla striata* Bruguière, 1792 (×3). 14. *Cerithium* sp. (×1). 15. *Ruditapes decussatus* (Linnaeus, 1758) (×1). 16. *Cerastoderma glaucum* (Bruguière, 1789). 17. *Ecrobia ventrosa* (Montagu, 1803) (×2). 18. *Abra alba* (W. Wood, 1802) (×7). 19–20. *Denropoma* sp. (×2). 21. *Dentalium dentalis* Linnaeus, 1758 (×2). 22. *Bittium reticulatum* (da Costa, 1778) (×1.5). 23. *Turbonilla acuta* (Donovan, 1804) (×2)

and by the presence of abundant pottery fragments (semi-rounded and angular) (Fig. 4). The basal contact of Fh is marked by a sharp erosional surface. This facies also displays large lithoclasts, wood and charcoal fragments, and several seeds (including grapes and olive pits; Fig. 7B, Fh). Coastal molluscs constitute up to 25%. The lagoonal gastropods reveal the dominance of *Abra alba* (40%) and *Bittium reticulatum* (20%). CaCO<sub>3</sub> and OM contents increase significantly (11–21% and 2.5–4%, respectively), the former reflecting a high concentration of bioclasts (shell fragments and gastropods). MS increases to a maximum value of  $8 \times 10^{-5}$  SI.

**Facies i (Fi):** the interval 78–55 cm dbs (90–55 cm dbs in TH1B), dated to 245–405 CE at 74–76 cm dbs and to 120–253 CE at 58–59 cm dbs, consists of a laminated, slightly sandy mud and sandy mud. Bioturbation (sand-filled holes) and a root in a vertical position were observed. CaCO<sub>3</sub> decreases up the unit from 12 to a minimum of 3%, and OM content continues to increase (5–7%). MS increases from  $8\text{--}22 \times 10^{-5}$  SI to a maximum of  $43 \times 10^{-5}$  SI. The base of this unit marks an upward change in sedimentation pattern, with sediments changing from essentially sandy to mostly muddy. This facies is marked by an increase in the fine fraction, which reaches up to 45% of the total sediment in TH1 and more than 55% in TH1B. Lagoonal molluscs (75%) are dominant and occur in association with marine gastropods.

**Facies j (Fj):** the interval 55–20 cm dbs (55–34 cm dbs in TH1B) contains brown-yellow, laminated, slightly sandy mud and mud and is marked by an increase in the fine fraction, which makes up to 90–97% of the total sediment. The middle part of this interval reveals the presence of abraded *Loripes*, gastropod fragments and continental plants. CaCO<sub>3</sub> remains fairly constant (7–9%), corresponding to bioclasts and calcite precipitation. The OM content continues to increase (9–12%), although these values could be influenced by the presence of Fe hydroxides which dehydrate at the temperatures used to estimate the OM and/or the clay content. MS varies between 13 and  $17 \times 10^{-5}$  SI.

**Facies k (Fk):** the interval from 20 cm dbs (34 cm dbs in TH1B) to the surface contains brown, laminated, slightly sandy mud and mud, and shows the highest values of marine elemental ratios (S/Al and Cl/Al) in the core. The upper few centimetres correspond to the present-day sedimentation, with roots (probably of *Salicornia*) in a vertical position. The CaCO<sub>3</sub> content is high (13–22%), corresponding to calcite precipitation. The OM content is the highest of all the cores (12–15%), although these values could be influenced, as in facies a and j, by the presence of Fe hydroxides that dehydrate at the temperatures used to estimate the OM content and/or the clay content. MS varies between 17 and  $26 \times 10^{-5}$  SI.

## TH2 core

Core TH2 is comparable in length to core TH1 (365 cm dbs) and consists of six sedimentary facies distinguished by their sedimentological, geochemical and malacological contents (Figs. 8, 9, 10).

**Facies 1 (F1):** the interval 365–242 cm (dbs) corresponds to a red terrigenous silty sand in which the fine fraction < 63 μm represents 30% of the total sediment. This depth interval is also characterised by the lowest marine elemental ratios values recorded in this core (Cl/Al, S/Al, Ca/Al and Sr/Al).

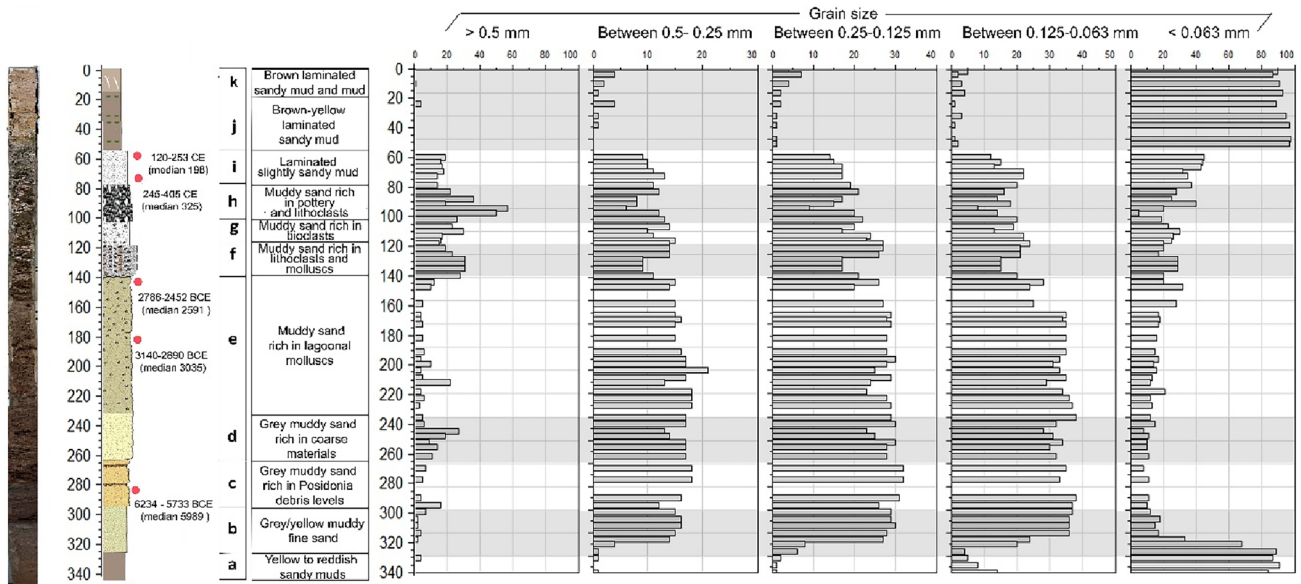
**Facies 2 (F2):** the interval 242–167 cm (dbs) consists of a grey sand rich in lithoclasts. The very coarse fraction (> 500 μm), almost absent in F1, reaches up to 30% of the total sediment. This interval is also characterised by an increase in marine (Cl/Al, S/Al and Ca/Al) and aeolian (Zr/Al, Ti/Al and Si/Al) elemental ratios. Only a thin layer of sediment at 220 cm dbs yielded mollusc macrofossils (represented by *Cerithium vulgatum*, *Turritella communis* and *Bittium reticulatum*), indicating the first signal of a marine intrusion at this site.

**Facies 3 (F3):** the interval 167–120 cm (dbs), before 2580–2198 BCE, is composed of grey sand. This facies also displays a reduction in the very coarse sand fraction and the first appearance of a diverse assemblage of molluscs at 130 cm, dominated (80%) by lagoonal species such as *Cerastoderma glaucum* and *Abra alba* and followed in abundance (20%) by marine taxa such as *Turritella* sp. and *Denropoma* sp. The elemental ratios Zr/Al, Ti/Al and Si/Al are the highest in this core and are indicative of an aeolian influence.

**Facies 4 (F4):** the interval 120–90 cm (dbs) has a peculiar facies with an erosive contact with the F3 sediments and corresponds to a bioclastic deposit. It is characterised by its richness in lithoclasts, probably eroded from Villafranchian outcrops, which are mixed with whole shells and shell fragments composed of coastal and lagoonal molluscs. The very coarse fraction (> 500 μm) reaches up to 35% of the total

**Table 2**  $^{14}\text{C}$  ages obtained from TH1, TH2 and TH5 cores

Core	Sample ID number	Material	Sample depth below surface (cm)	Conventional $^{14}\text{C}$ age (yr BP)	$\delta^{13}\text{C}$ (‰)	Age (cal yr BCE/CE)
TH1	COL7388.1.1	Charcoal	58–59	$1844 \pm 34$	NA	120–253 CE (90.1%) 290–319 CE (5.4%) (median 198 CE)
	COL7389.1.1	Charcoal	74–76	$1757 \pm 35$	NA	245–405 CE (95.4%) (median 325 CE)
	COL7390.1.1	Charcoal	145–147	$4043 \pm 70$	NA	2874–2794 BCE (12.3%) 2786–2452 BCE (81.1%) 2421–2406 BCE (0.8%) 2376–2352 BCE (1.3%) (median 2591 BCE)
	COL7391.1.1	Plant/wood	181–183	$4382 \pm 71$	NA	3334–3213 BCE (18.0%) 3191–3147 BCE (5.1%) 3140–2890 BCE (72.3%) (median 3035 BCE)
	COL7392.1.1	Plant/wood	286–288	$7120 \pm 128$	NA	6234–5733 BCE (95.4%) (median 5989 BCE)
TH2	COL7393.1.1	Plant/wood	115–123	$3817 \pm 72$	NA	2580–2198 BCE (94.5%) 2168–2149 BCE (1.0%) (median 2394 BCE)
TH5	COL7717.1.1	Plant/wood	62–64	$703 \pm 40$	-5.8	1464 – 1828 CE (median 1635 CE)
	COL7718.1.1	Bulk organic sediment	166–168.5	$2637 \pm 45$	-3.9	656–650 BCE (0.3%) 640–177 BCE (95.2%) (median 396 BCE)
	COL7719.1.1	Bulk organic sediment	300–302	$6108 \pm 47$	-13.5	4739–4346 BCE (95.4%) (median 4547 BCE)

**Fig. 3** Sedimentological data for core TH1, with core photos, log, depth of the core below the surface (cm), calibrated dates in BCE/CE (95.4% interval) and median age CE or BCE, facies types, and grain size (mm) distributions

sediment. The first appearance of the marine taxa *Retusa* sp., *Nassarius sufflatus* and *Turbonella* sp. is observed in this

facies. F4 is also characterised by high values of the marine elemental ratios  $\text{Cl}/\text{Al}$ ,  $\text{S}/\text{Al}$ ,  $\text{Ca}/\text{Al}$  and  $\text{Sr}/\text{Al}$ .

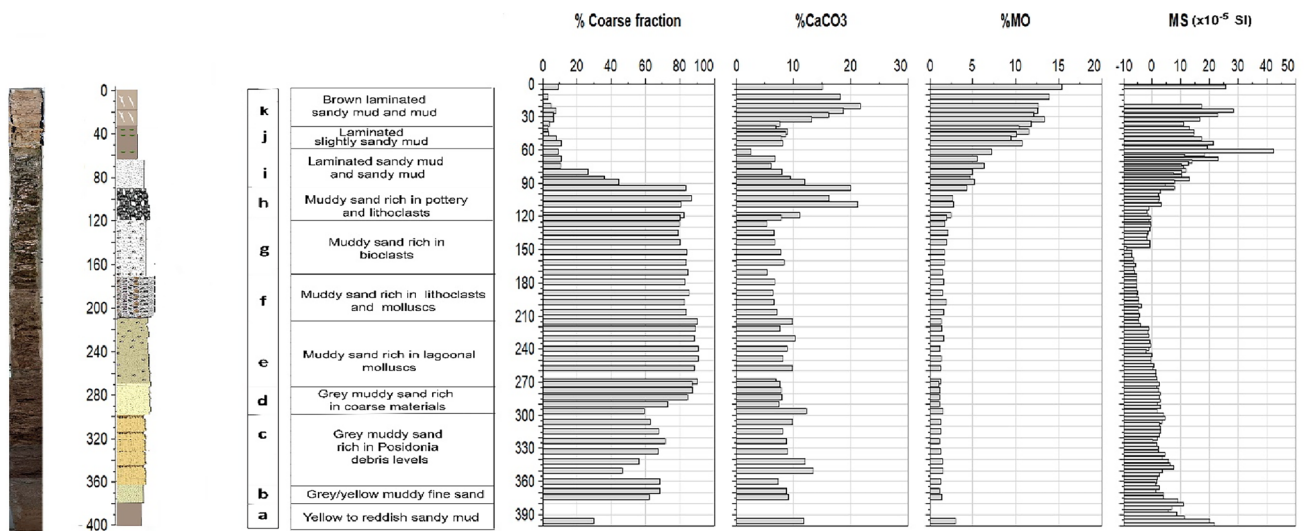


**Fig. 4** Sedimentological data for core TH1B, with photo, log and depth of the core below the surface (cm) as well as facies types, coarse (>63 μm) fraction, CaCO<sub>3</sub> and organic matter contents, and magnetic susceptibility (× 10<sup>-5</sup> SI) as functions of depth

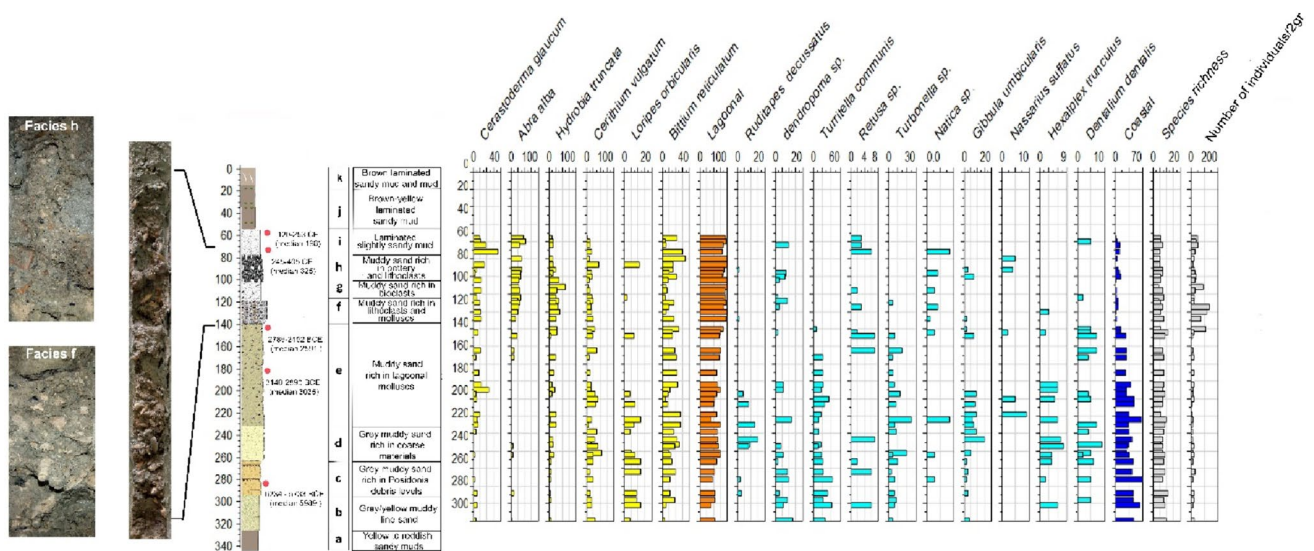


**Fig. 5** Species richness and the density and abundance (number of individuals/2 gr) of each of the main mollusc species of core TH1. Photos of the core, log, depth of the core below the surface (cm) and described facies. Calibrated dates in BCE/CE (95.4% interval) and median ages

*Facies 5 (F5)*: the interval 90–30 cm (dbs) is composed of a succession of fine sand, silt and green clay. Only a few shells of *C. glaucum* and *H. truncata* were found in the fine sand layers; the other layers were barren. The fine fraction (<63 μm) makes up to 95% of the total sediment. Facies F5 revealed high values of the detrital elemental ratios Rb/Al and Fe/Al in association with remarkable reductions in the marine (Cl/Al, Ca/Al and Sr/Al) and aeolian (Zr/Al and Si/Al) elemental ratios.

*Facies 6 (F6)*: the interval between 30 cm (dbs) and the surface is made up of red silt rich in plant debris,

with *Hydrobia truncata* at 10 and 2 cm (dbs). It records improvements in the marine (Ca/Al, S/Al, Sr/Al and Cl/Al) and aeolian (Zr/Al, Ti/Al and Si/Al) elemental ratios. We also noted a reduction in the fine fraction in this interval, except for the top 5 cm (Fig. 8).

**TH4 core**

Core TH4 is 320 cm long, comparable to TH1 (340 cm) and TH2 (360 cm), but less rich in molluscs. It consists of six

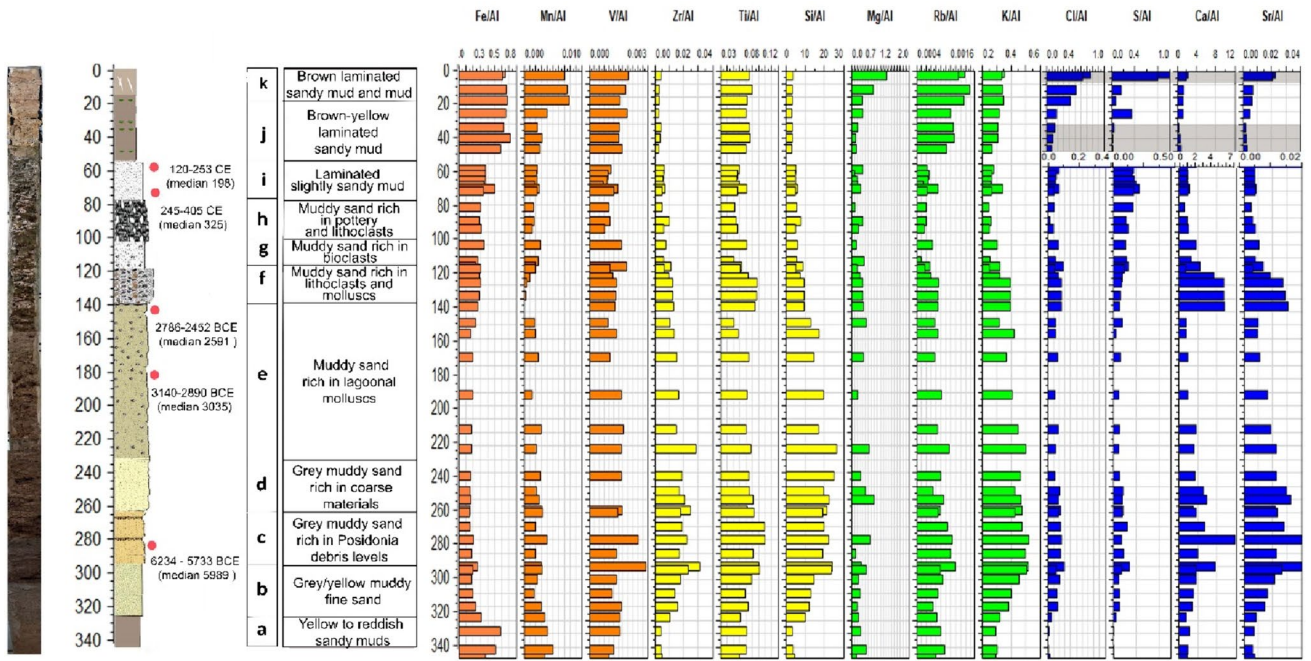


**Fig. 6** Geochemical data for core TH1. Al-normalised concentrations of elements used as fluvial, aeolian and marine indicators. Core photo, log, depth of the core below the surface (cm) and described facies. Calibrated dates in BCE/CE (95.4% interval) and median ages

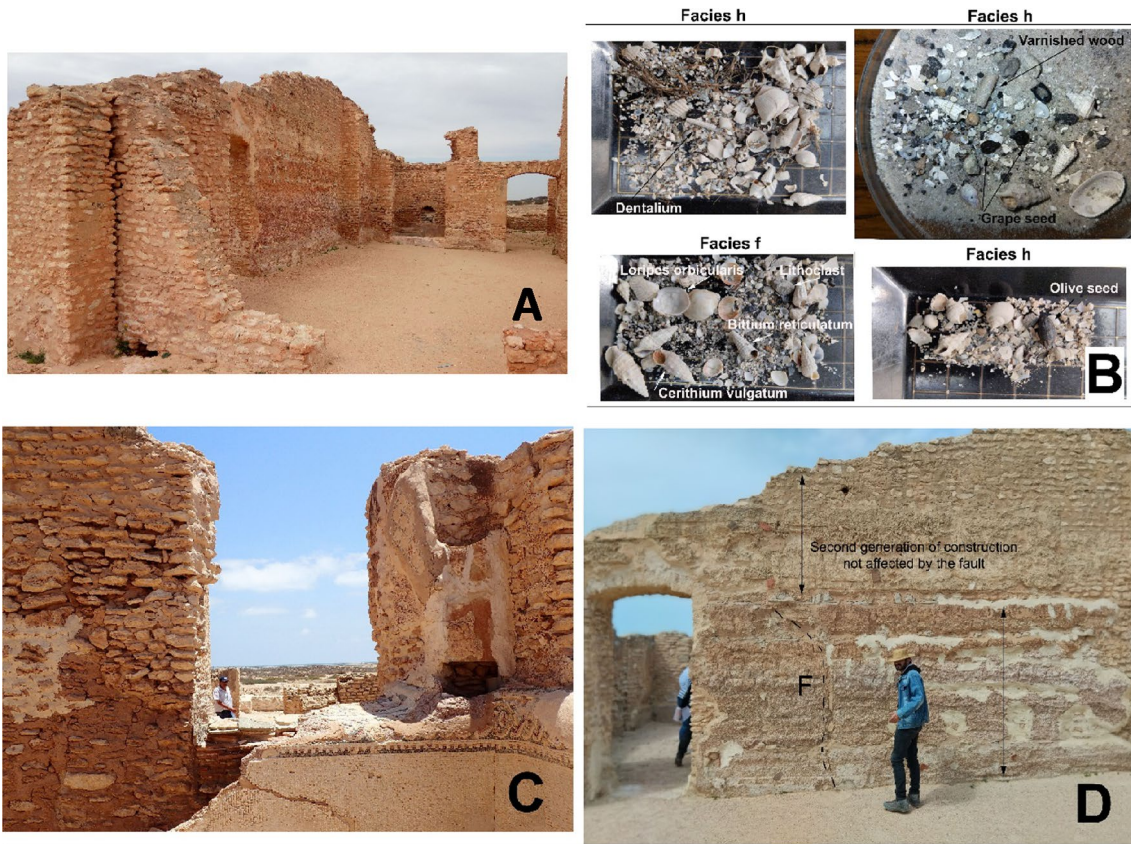


**Fig. 7** **A, C** Double wall in the archaeological city of Thyna. **B** Facies (Ff and Fh) of the TH1 core, showing different elements and molluscs. **D** Two generations of wall construction in the archaeological city of Thyna; a fault (F) can be seen

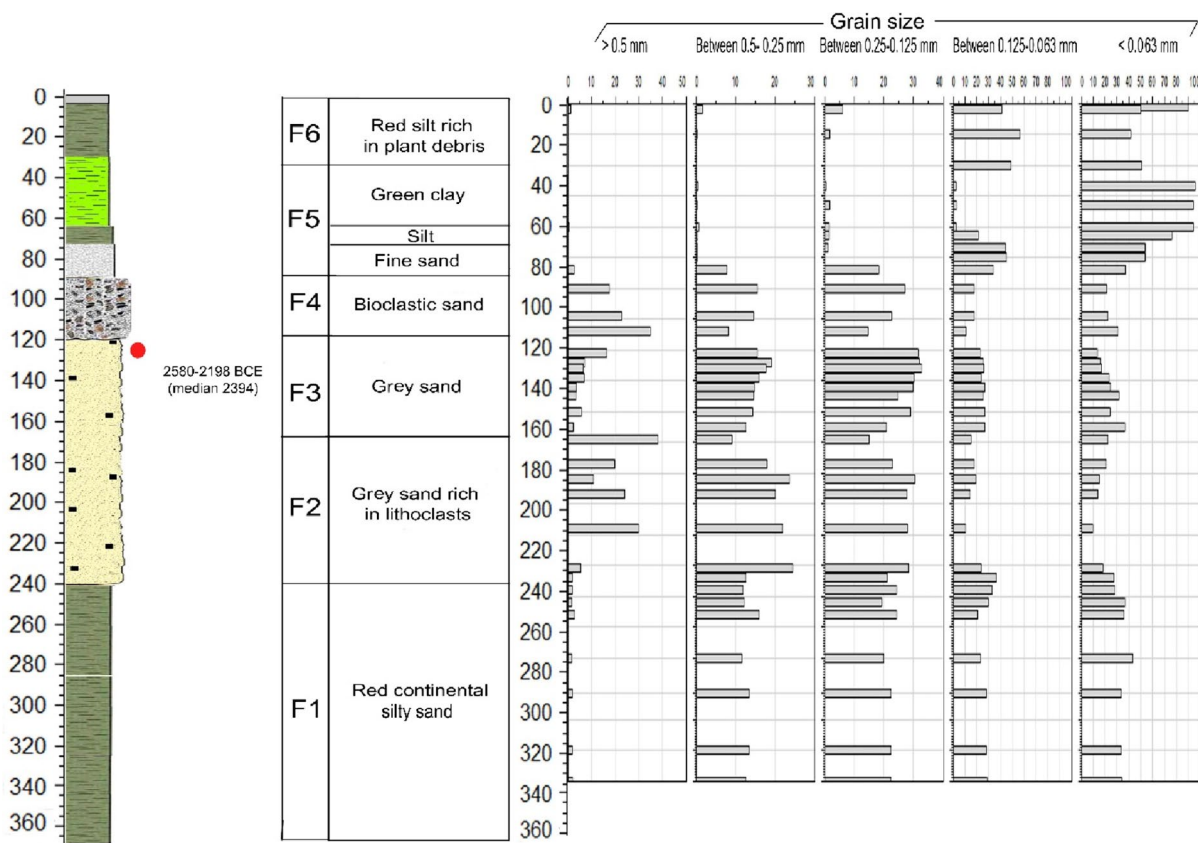


Fig. 8 Sedimentological data for core TH2. Log, depth of the core below the surface (cm), calibrated dates in BCE/CE (95.4% interval) and median ages, facies types, and grain size (mm) distributions

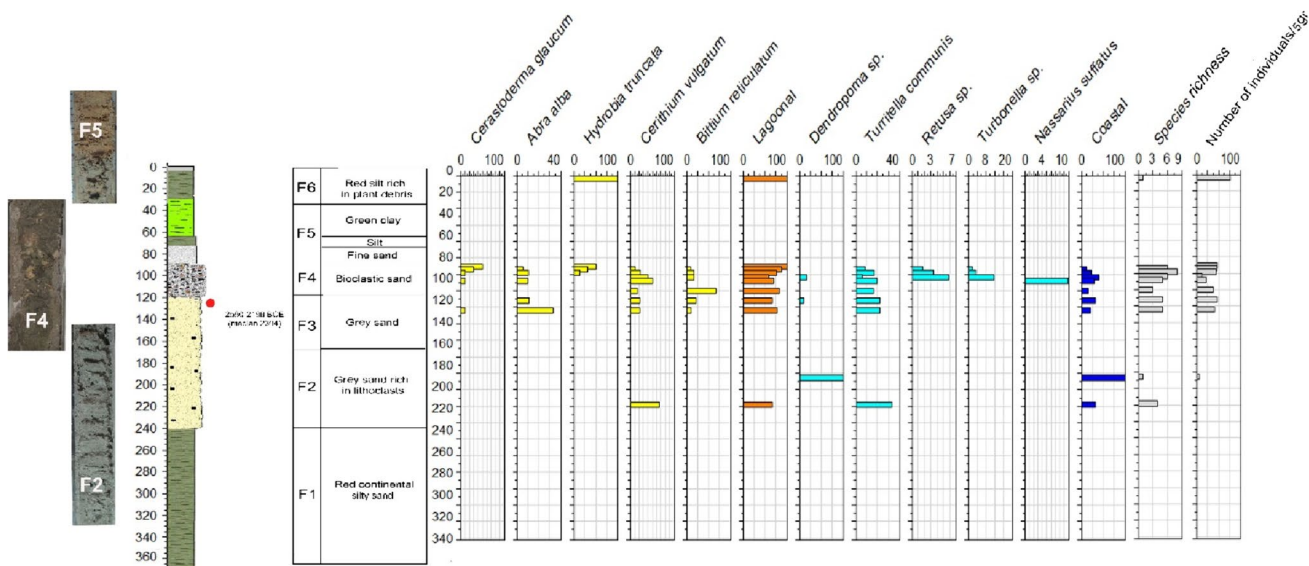
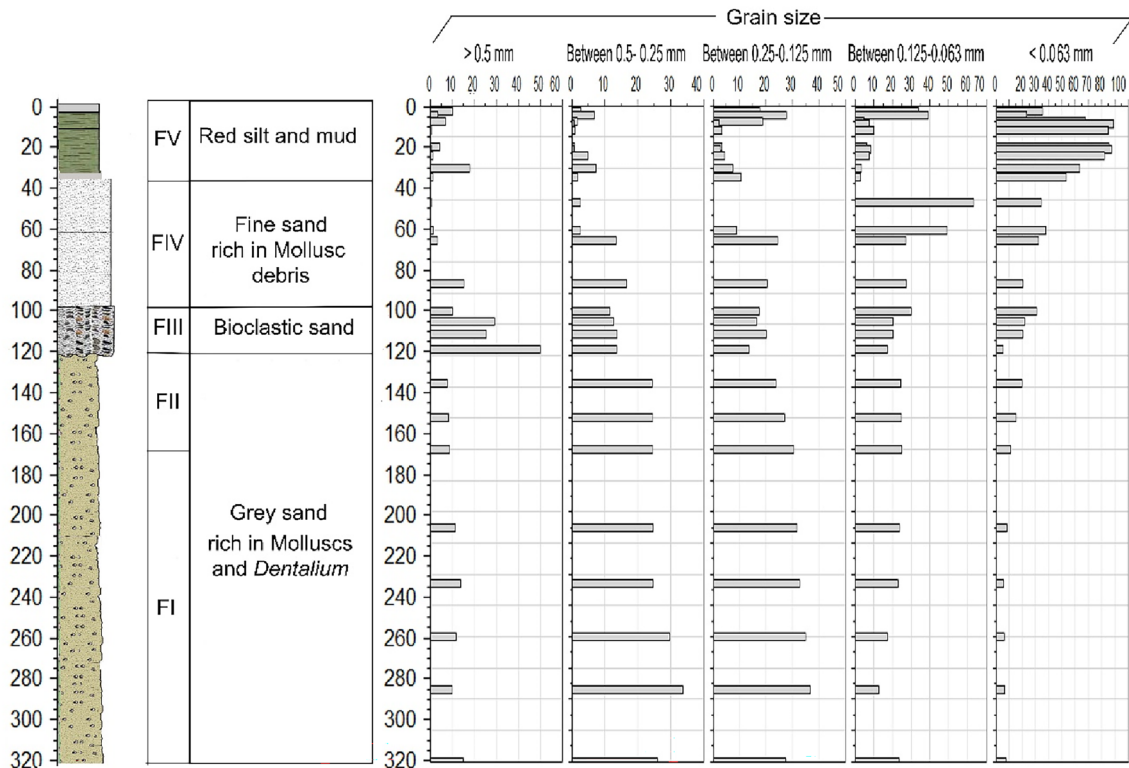


Fig. 9 Species richness and the density and abundance (number of individuals/5 gr) of each of the main mollusc species of core TH2. Photos of facies F2, F4 and F5; log, depth of the core below the sur-

face (cm) and described facies. Calibrated dates in BCE/CE (95.4% interval) and median ages



**Fig. 10** Geochemical data for core TH2. Al-normalised concentrations of elements used as fluvial and aeolian input and marine indicators. Log, depth of the core below the surface (cm) and facies types



**Fig. 11** Sedimentological data for core TH4: log, depth of the core below the surface (cm), facies types and grain size (mm) distributions

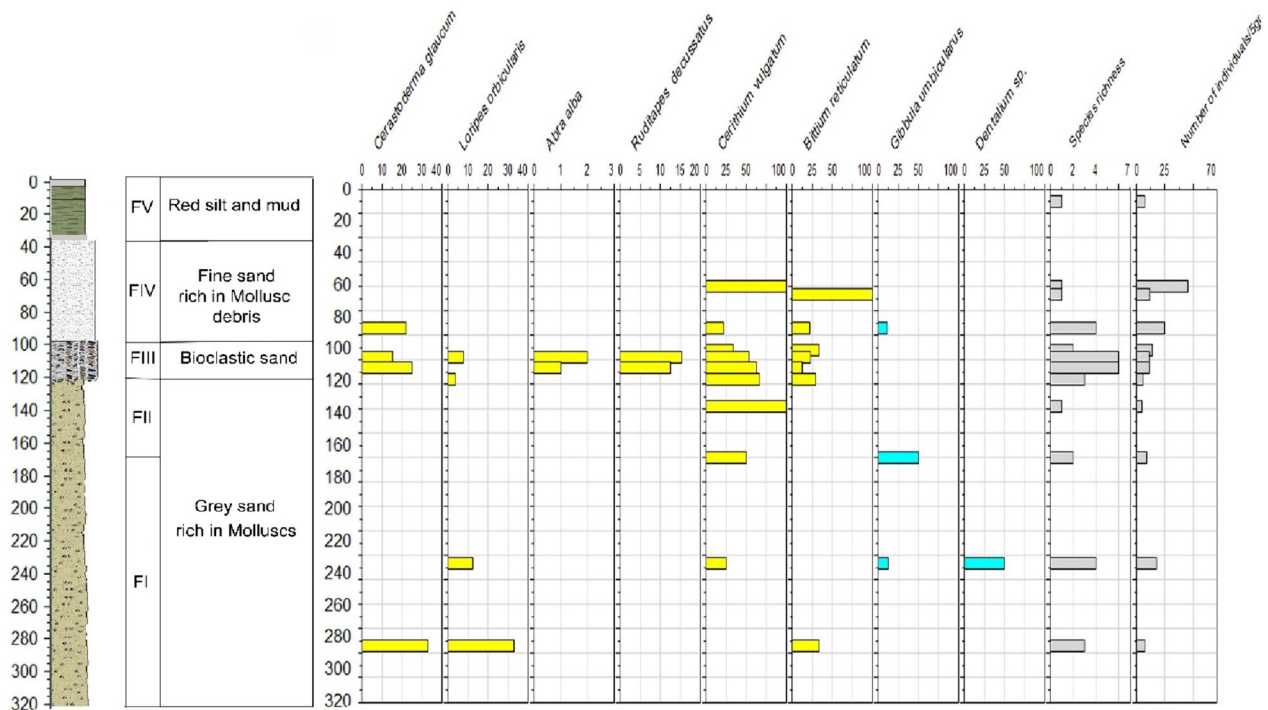


**Fig. 12** Species richness and density and abundance (number of individuals/5 gr) of each of the main mollusc species of core TH4. Log, depth of the core below the surface (cm) and described facies

sedimentary facies, which differ in their sedimentological and malacological contents (Figs. 11, 12).

**Facies I (FI):** the interval 320–167 cm (dbs) corresponds to a grey sand in which the fine fraction (< 63  $\mu\text{m}$ ) does not exceed 10% of the total sediment. This facies is characterised by the occurrence of *Posidonia* sp., mollusc shell fragments, complete shells of *Dentalium* sp., and rare occurrences of *Cerithium vulgatum* and *Loripes orbiculatus*.

**Facies II (FII):** the interval 167–121 cm (dbs) consists of grey sand rich in lithoclasts and mollusc debris but poor in *Posidonia* remains. The molluscs include complete shells of *Cerithium vulgatum* and *Gibbula* sp. The fine fraction increases with respect to the underlying sediment and reaches up to 20%.

**Facies III (FIII):** the interval 120–100 cm (dbs) consists of bioclastic sands similar in texture and composition to the facies described for cores TH1 (Ff) and TH2 (F4). Shell debris makes up 50% of the total sediment and forms the majority of the > 500  $\mu\text{m}$  size fraction. The sediment contained in this facies is characterised by an erosive surface at the base. Lagoonal molluscs include intact *Cerithium vulgatum* (dominant), *Bittium reticulatum* and rare *Loripes orbiculatus*. Several shells of *Cerithium* sp. and *Ruditapes decussatus* are bio-eroded. Facies III also shows a strong

increase in the > 500  $\mu\text{m}$  size fraction (reaching up to 50% of the total sediment in the lower half of the layer), but this size fraction decreases in proportion further up (Fig. 11), and the sediment hosts unique specimens of bivalves (*Abra alba* and *Ruditapes decussatus*).

**Facies IV (FIV):** the interval 100–30 cm (dbs) consists of fine sand rich in mollusc debris and contains only a few whole shells of *Cerastoderma glaucum*, *Cerithium vulgatum* and *Bittium reticulatum*. Between 60 to 30 cm dbs, the sediment was found to be devoid of molluscs. The fine fraction (< 63  $\mu\text{m}$ ) reaches up to 30% of the total sediment.

**Facies V (FV):** the interval from 30 cm to the surface is composed of red silt and clays rich in both living and dead plants. Mollusc shells are absent in this interval.

### TH5 core

Core TH5 has a total length of 400 cm and consists of nine sedimentary facies distinguished by their sedimentological characteristics.

**Facies A (FA):** the interval 400–373 cm (dbs) corresponds to the basement and is probably Upper Pleistocene in age. It is characterised by yellow carbonated azoic sandy mud or muddy sand (maximum  $\text{CaCO}_3$  of 15%), with the sand component being fine or very fine and moderately well sorted.

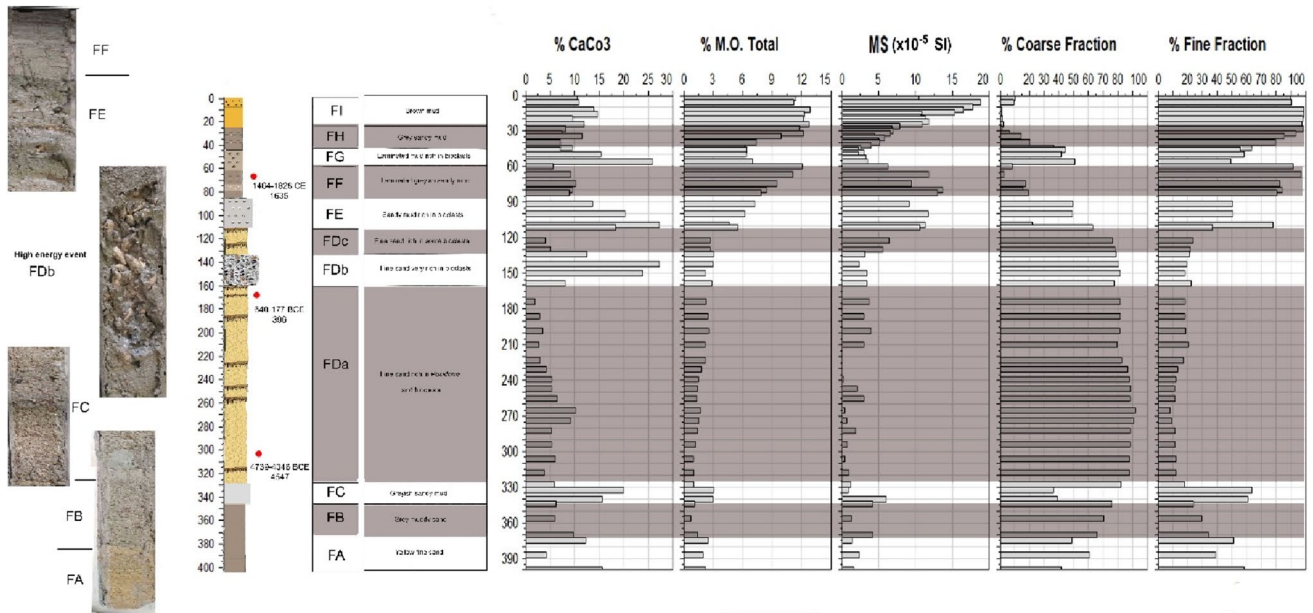


**Fig. 13** Sedimentological data for core TH5. Photos of parts of the core, the log, the depth of the core below the surface (cm), facies types, calibrated dates in BCE/CE (95.4% interval), and median ages.

The values of organic matter (about 2%) and magnetic susceptibility are low (Fig. 13); the former is probably related to the presence of Fe hydroxides.

**Facies B (FB):** the interval 373–342 cm (dbs), which most probably corresponds to the basement, also consists of grey muddy to slightly muddy azoic sand ( $\text{CaCO}_3$  between 6% and 10%). The  $> 63 \mu\text{m}$  fraction is a fine and moderately to moderately well-sorted sand with low organic matter ( $< 1.5\%$ ) and magnetic susceptibility values.

**Facies C (FC):** the interval 342–30 cm (dbs) consists of a compact, greenish carbonated sandy mud with moderately high  $\text{CaCO}_3$  values (16–20%) and a 3% OM content.

**Facies D (FD):** the interval 330–112 cm (dbs) consists of slightly muddy sand (coarse fraction essentially above 80%) and can be divided into three sub-facies.

**Sub-facies Da (FDa):** the interval 330–160 cm (dbs) was deposited before 4739–4346 BCE (radiocarbon date at ca. 301 cm dbs) and ended at approximately 640–177 BCE (radiocarbon date at ca. 167 cm dbs). It consists of 1.7 m of fine and usually moderately sorted sand, with some levels containing fibers of *Posidonia*, especially at 274, 257, 233 and 190 cm (dbs). The organic matter content varies between 1% and 2.5% but consistently increases to the top. Bioclasts (shells and shell fragments) are present in all of this sub-unit but are concentrated at 253–276 cm dbs. The  $\text{CaCO}_3$  content ranges between 7–10%. Bivalve and gastropod shells (*Cerithium vulgatum*) are present in this interval. Magnetic susceptibility is low but increases upwards in this sub-facies.

Coarse ( $> 63 \mu\text{m}$ ) and fine ( $< 63 \mu\text{m}$ ) fractions,  $\text{CaCO}_3$  and organic matter contents and magnetic susceptibility ( $\times 10^{-5}$  SI) variation

**Sub-facies Db (FDb):** the interval 160–132 cm (dbs) is formed by grey medium and poorly sorted sand. Due to the high concentration of bioclasts (whole bivalves and gastropods, *Cerastoderma* and *Cerithium vulgatum*), the maximum  $\text{CaCO}_3$  content reaches values of up to 27%. The OM content varies between 2% and 3% in this interval.

**Sub-facies Dc (FDc):** the interval 132–112 cm (dbs) is composed of grey fine and poorly sorted sand and contains some bioclasts ( $\text{CaCO}_3$  content 4–5%). MS increases upwards, and the OM content is around 3%.

**Facies E (FE):** the interval 112–83 cm (dbs) consists mainly of sandy mud with a high content of bioclasts (whole shells and shell fragments of various species of bivalves and gastropods (*Cerithium vulgatum*)). The  $\text{CaCO}_3$  varies between 14% and 27%. Layers with a higher bioclast content in the  $> 63 \mu\text{m}$  fraction are represented by medium and poorly sorted sand. Levels with a lower bioclast content are mainly fine and poorly sorted sands. Due to the nature of sediment, the OM increases from 5% to 7% along this facies. MS is higher than in the previous facies, with values between 7 and  $12 \times 10^{-5}$  SI. The base of this facies marks an upward change in the sedimentation pattern, with sediments changing from fine sands (FD) to mainly muddy materials (FE).

**Facies F (FF):** the interval 83–58 cm (dbs) is composed of greenish/greyish slightly sandy mud to mud (fine fraction of between 81% and 97%), is laminated above 69 cm dbs, and includes dark layers of OM (8–12%). Bioclasts are present, and the  $\text{CaCO}_3$  content varies



between 6% and 10%. The upper part of this facies dates to 1464–1828 CE.

**Facies G (FG):** the interval 58–45 cm dbfs is composed of grey laminated mud, with bioclasts concentrated at the base (higher concentrations of *Cerithium vulgatum* and bivalves at 54–58 cm dbfs; maximum  $\text{CaCO}_3$  of 26%). The values of OM and MS decrease upwards. The coarse fraction (around 40–50%) is classified as fine-to-coarse poorly to very poorly sorted sand, where textural changes are mainly due to the bioclast content.

**Facies H (FH):** the interval 45–30 cm (dbfs) consists of laminated grey slightly sandy mud and contains thin laminated sand layers and other levels enriched in *Posidonia* debris. Organic matter increases from 6% to 12%, and  $\text{CaCO}_3$  varies from 7% to 12% in this interval.

**Facies I (FI):** the interval from 30 cm to the top consists of azoic brown mud and shows the highest OM content (12–13%). Macroscopic examination, however, revealed no evidence of organic matter, suggesting that this is due to analytical limitations (water loss associated with the high clay content during laboratory OM measurements or the presence of Fe hydroxides that dehydrate at the temperatures used to estimate OM content).  $\text{CaCO}_3$  varies between 8% and 15%. Magnetic susceptibility increases to the highest values in this core. The upper 8.5 cm is slightly coarser (coarse fraction about 10%), corresponding to a brown slightly muddy sand.

## Foraminifera and facies types

A total of 10,000 benthic foraminifera, belonging to 11 genera and 21 species, were picked from 24 samples of core TH1, 25 samples of TH4, and 16 samples of TH2. In all cores analysed, five species represent more than 5% of the picked foraminifera, including *Ammonia veneta* (35%), *Ammonia aberdoveyensis* (18%), *Elphidium jensenii* (6%), *Hauerina* sp. 1 (8%) and *Ammonia parkinsoniana* (6%). In general, foraminifera tests are well preserved, with hardly any visible signs of abrasion or damage. Exceptions include specimens found in facies Ff (TH1 core), facies F4 (TH2 core) and facies FIII (TH4 core), where the species *Ammonia veneta* and *Haynesina germanica* are frequently fragmented.

In core TH1, the numerical abundances of foraminiferal biotas decrease in facies Fb to Fe (from 125 to 75 individuals/1 gr), and they are absent in facies Fa and scarce in Ff. They increase from Fg to Fj, reaching up to 2000 individuals/1 gr. The number of species ranges from 1 to 15 in most samples (Fig. 14). Facies Ff to Fi record the dominance of the ammoniids, while Fb to Fd are marked by a mixture of ammoniids (30%), elphidiids (30%), miliolids (35%) and rosalinids (2%). Peneroplids reach up to 4% in facies Fj, where they are associated with miliolids (70%) and rosalinids (3%).

In core TH4 (Fig. 15), the number of individuals decreases from facies FI to FIV. In facies FV, on the other hand, the number of foraminifera increases to the maximum

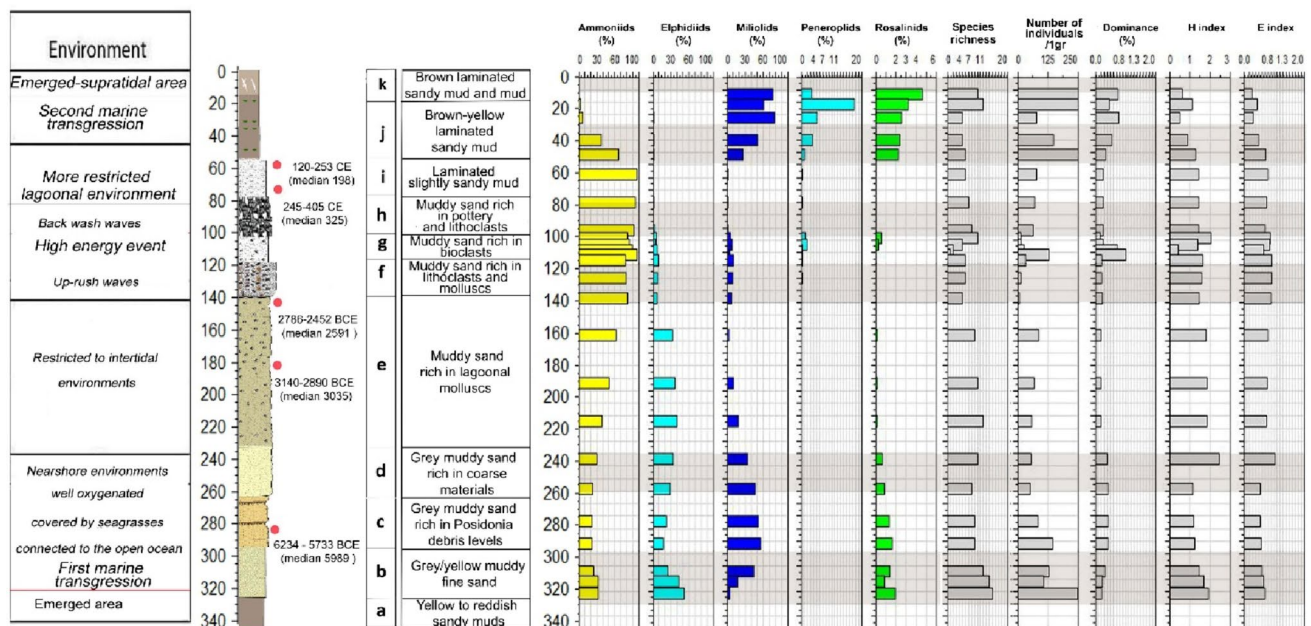


**Fig. 14** Main foraminifera ecologic group species of core TH1, species richness, abundances (number of individuals/1 gr), dominance and diversity indices (Shannon,  $H$  and equitability,  $E$ ). Log, depth

below the surface (cm), calibrated dates in BCE/CE (95.4% interval) and median ages, facies types, and interpreted environments

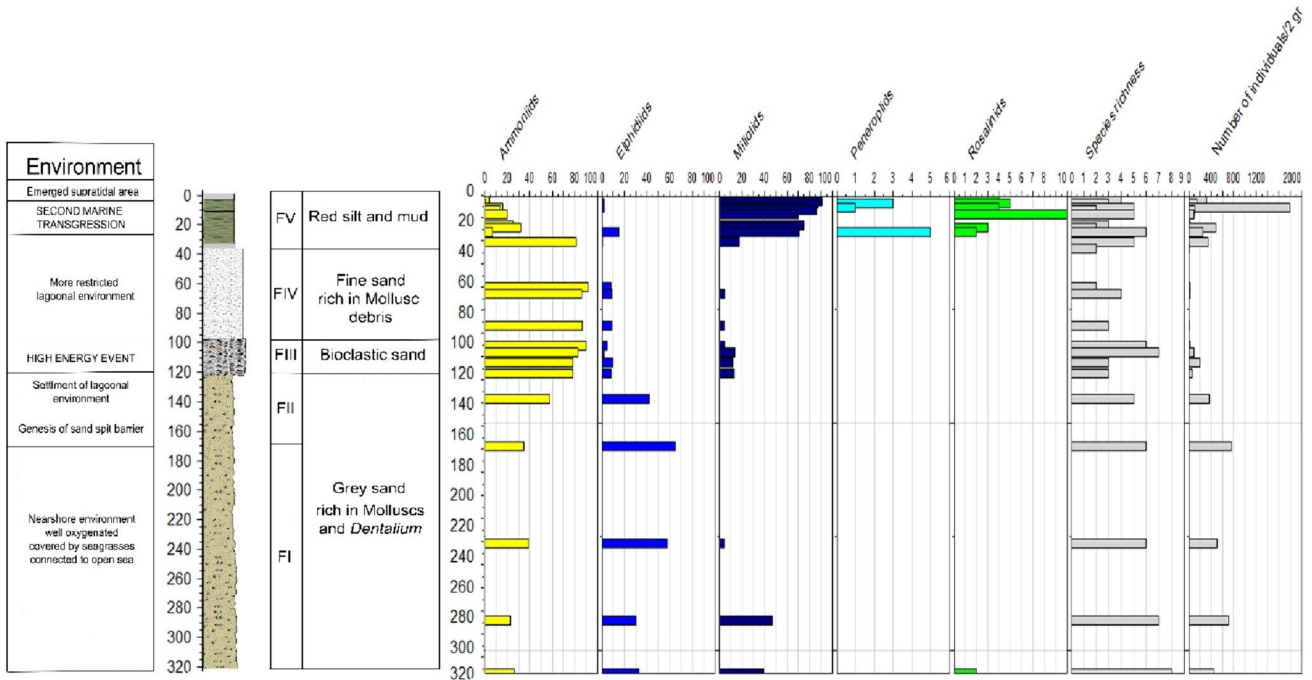


**Fig. 15** Main foraminifera ecologic group species of core TH4, species richness and abundances (number of individuals/2 gr). Log, depth below the surface (cm), facies types and interpreted environments

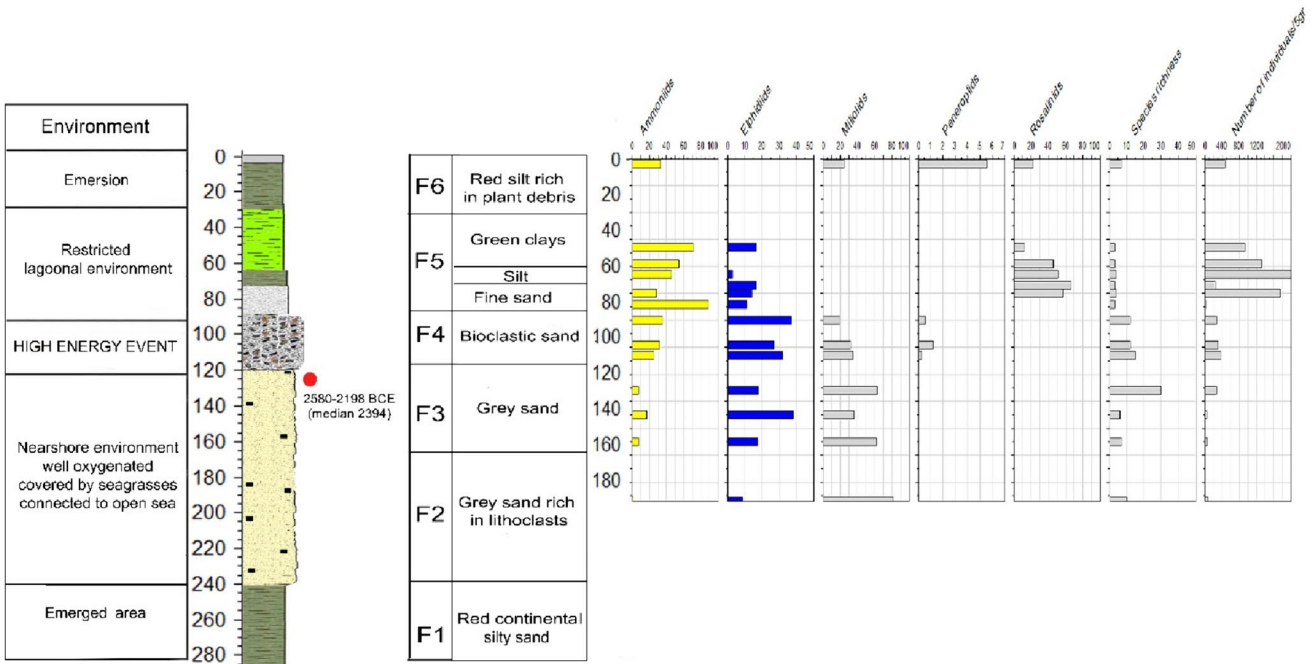
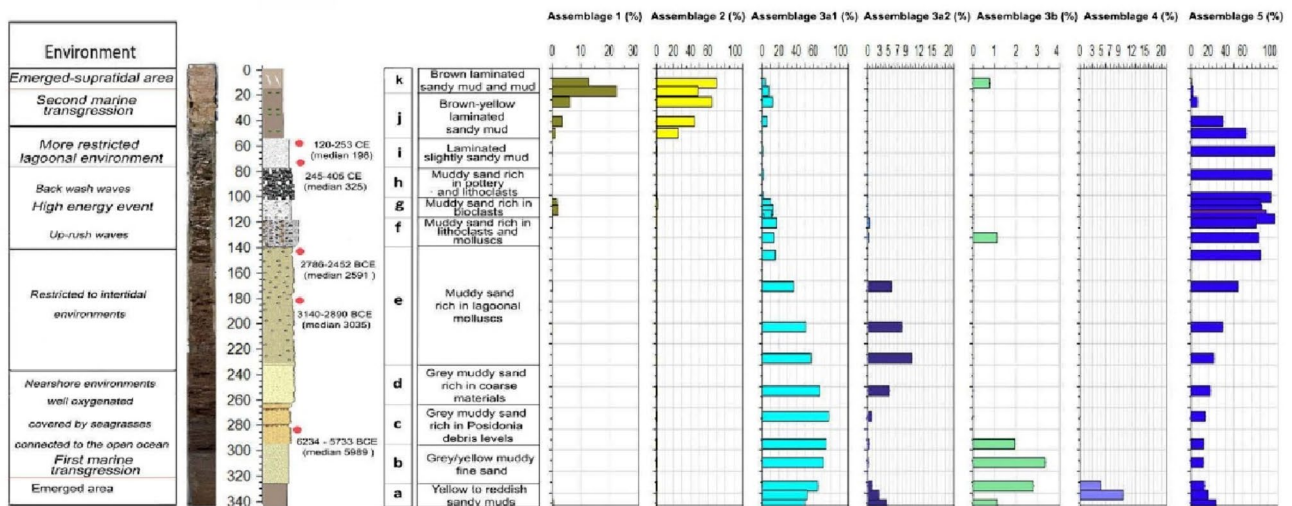


**Fig. 16** Main ecological foraminifera groups in core TH2. Species richness and abundances (number of individuals/5 gr). Log, depth below the surface (cm), calibrated dates in BCE/CE (95.4% interval) and median ages, facies types, and interpreted environments

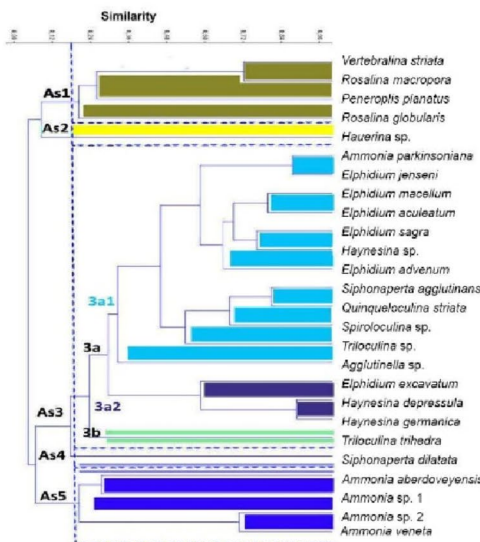
value (2000 individuals at 5 cm). Ammoniid foraminifera dominate in facies FIII and FIV (90%). FII is characterised

by a mixture of ammoniids (40%) and elphidiids (60%), with miliolids also occurring in the lower part of FI.

A



B



C

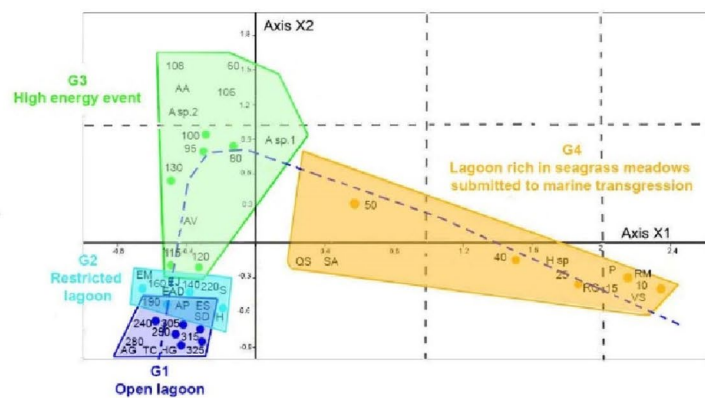


**Fig. 17** Statistical analyses based on benthic foraminifera. **A** Vertical variations in the relative abundances of the five foraminiferal assemblages. **B** Species group R-mode cluster analysis showing main foraminiferal assemblages (As1–As5). **C** Correspondence analysis: projection of both foraminifera data and samples in the 1 × 2 factorial plane for core TH1. *Agglutinella* sp. (AG), *Ammonia parkinsoniana* (AP), *Ammonia veneta* (AV), *Ammonia* sp. 1, (*A. sp.1*), *Ammonia* sp. 2, (*A. sp.2*), *Ammonia aberdoveyensis* (AA), *Elphidium aculeatum* (Ea),

*Elphidium advenum* (EAD), *Elphidium excavatum* (Eex), *Elphidium jenseni* (EJ), *Elphidium sagra* (ES), *Elphidium macellum* (EM), *Hauerina* sp. (*Hsp*), *Haynesina depressula* (Hd), *Haynesina germanica* (Hg), *Haynesina* spp. (*Hsp*), *Peneroplis planatus* (P), *Quinqueloculina striata* (QS), *Rosalina globularis* (RG), *Rosalina macropora* (RM), *Siphonaperta agglutinans* (SA), *Siphonaperta dilatata* (SD), *Spiroloculina* sp. (Sp), *Triloculina costa* (TC) and *Vertebralina striata* (V)

Core TH2 (Fig. 16) differs from the other two cores by the increases in diversity and the number of individuals from F2 to F4. These two facies are marked by a dominance of elphidiids (30%) and miliolids (60%) associated with ammoniids (10%). However, facies F5 records the highest number of individuals and a decrease in diversity. The upper parts

of F5 and F6 are azoic except for one level at 2 cm below the surface.

### Statistical analysis

Five foraminiferal assemblages were differentiated according to the R-mode cluster analysis of TH1 (Fig. 17A, B),

while k-means cluster and statistical analysis using the elbow method indicated that the optimal number of clusters was four. The k-means cluster analysis revealed clear faunal transitions by delineating the core samples into four clusters with different ecological meanings. The top four samples aggregated in cluster 1 (10–40 cm), while core samples from 95 to 105 cm constituted cluster 2. Core samples between 45 and 90 cm shared considerable faunal similarities with the bottom of the core between 195 and 325 cm, which were grouped together as cluster 4. On the other hand, the middle part of the core between 110 and 160 m was characterised by two alternating faunas of cluster 3 and cluster 4.

Assemblage 1 (As1) comprises *Vertebralina striata*, *Rosalina macropora*, *Peneroplis planatus* and *Rosalina globularis*. These taxa are present in Fj and Fg (2.5%), reaching up to 20% in the transition between Fj and Fk, and are present in Fk (12%). The other samples contain only a few individuals of these species.

Assemblage 2 (As2) is monospecific (*Hauerina* sp.) and is present in the lower part of facies Fj (30%) and in facies Fj and Fk, where it represents more than 60% of the total foraminiferal assemblage.

Assemblage 3a (As3a) can be divided into two sub-assemblages. Assemblage 3a1 contains *Ammonia parkinsoniana*, *Elphidium jenseni*, *Elphidium macellum*, *Elphidium aculeatum*, *Elphidium sagra*, *Haynesina* sp., *Elphidium advenum*, *Siphonoperta agglutinans*, *Quinqueloculina striata*, *Spiroloculina* sp., *Triloculina* sp. and *Agglutinella* sp. The assemblage is dominant in facies Fb, Fc and Fd (60%), abundant in most samples of Fa and Fe (40%), and rare in Ff (20%), Fg (10%), Fh (5%), Fi (5%), Fj (10%) and Fk (7%). Assemblage 3a2 contains *Elphidium excavatum*, *Haynesina depressula* and *Haynesina germanica*. The assemblage constitutes 9% in facies Fe and Fd, is less dominant in facies Ff and Fa (2% and 5%), and is absent from Fg to Fk.

Assemblage 3b (As3b) is monospecific (*Triloculina trihedra*). It is present in facies Fb (3%) and in Fa, Ff and Fk (1%). Assemblage 4 (As4) is monospecific (*Siphonoperta agglutinans*) and is present in Fa only (9%). Assemblage 5 (As5) includes *Ammonia veneta*, *Ammonia aberdoveyensis*, *Ammonia* sp. 1 and *Ammonia* sp. 2. This assemblage makes up 20% of facies Fa. It increases in facies Fe (50%), and is dominant in Ff to Fi (up to 90%). It decreases in Fj (40%) and is rare in the upper part of facies Fj (5%).

### Correspondence analysis (CA) (Fig. 17C)

To determine the structure in our foraminiferal data set, a correspondence analysis (CA) was carried out by using foraminiferal abundances present in individual sampling levels of core TH1 (Fig. 17C). The factorial plane plot reveals four clouds of sampling points that are

arranged along a parabolic curve reflecting a gradient of environmental energy levels (Benzécri 1980; Zaïbi et al. 2011).

Group 1 (G1), located at the negative poles of axes X1 and X2, includes all samples from facies Fa to Fd and is characterised by the highest species richness and diversity. This group includes *Agglutinella* sp., *Triloculina* sp., *Haynesina germanica*, *Ammonia parkinsoniana*, *Elphidium sagra*, *Haynesina depressula*, *Elphidium excavatum*, *Triloculina trihedra* and *Elphidium aculeatum* and is considered to be typical of an open lagoon environment (Trubin et al. 2023).

Group 2 (G2) includes samples of facies Fe and is characterised by a reduction in the number of species and a slight increase in the number of individuals. *Elphidium jenseni*, *Elphidium macellum*, *Spiroloculina* sp., *Haynesina* sp., *Elphidium advenum* and *Siphonoperta dilatata* are found in this group. The lower number of species and the composition of group G2 indicates that the environmental conditions became more restricted.

Group 3 (G3), situated at the positive end of axis X2, contains samples of the bioclastic facies Ff and samples of Fg. It is characterised by a rapid increase in the number of species and by the presence of brackish indicator taxa such as *Ammonia aberdoveyensis*, *Ammonia veneta*, *Ammonia* sp. 1 and *Ammonia* sp. 2. The dominance of ammoniid taxa indicates the presence of additional environmental stressors, including brackish and/or high-energy conditions.

Group 4 (G4) contains typical epiphytes, including *Rosalina globularis*, *Rosalina macropora*, *Vertebralina striata*, several miliolids (*Hauerina* sp., *Siphonoperta agglutinans* and *Quinqueloculina striata*) and the symbiont-bearing miliolid *Peneroplis planatus*. This assemblage characterises facies Fk and Fj and is indicative of phytal covered habitats, including seagrass and algal meadows under normal marine conditions (e.g. open lagoons and nearshore coastal habitats; Langer 1988, Trubin et al. 2023).

The CA analysis shows a distinct separation of the G1 and G4 groups, where G1 species characterise lagoonal environmental conditions and species of G4 species mark the initiation of a transgression. Group G3 is located at an intermediate position between G1 and G4. This group is present in coarse bioclastic-rich sediment levels and contains indicator taxa that characterise stressful nearshore conditions that were subjected to a high-energy event.

### Discussion: evolution of the Thyna coast

During the Late Pleistocene–Early Holocene, the deposition of azoic sandy muds (Fa, TH1 core), silty sands (F1–F2, TH2 core) and yellow sandy muds (FA and FB and probably FC, TH5 core) prevailed. These sediments are continental

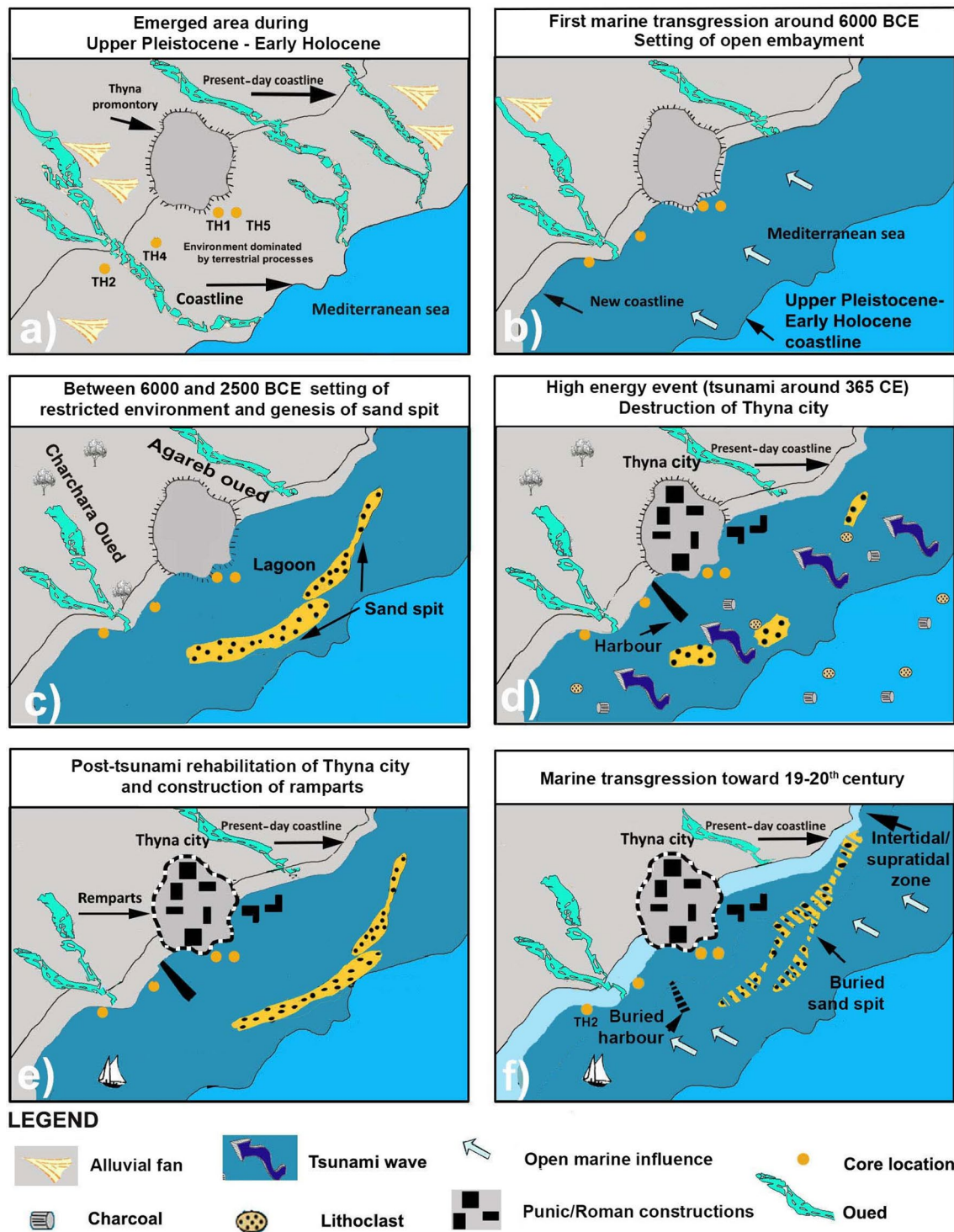


**Fig. 18** Schematic representation of the environmental evolution of the Thyna coast, as inferred from micropaleontological and sedimentological core data

in origin and represent proximal drainage areas of wadi habitats (=oueds) along alluvial plains (e.g. Charchara, Agareb and other rivers; Figs. 1C, 18a). Following the first marine transgression (around 6000 BCE), the depositional

environment has subsequently evolved into a coastal environment with open bays (Fig. 18b). This transformation is recorded by sediments and faunal components of facies Fb-c, F3, FI and FDa (cores TH1, TH2, TH4, TH5). Facies

Fc contains common coastal molluscs, with *Turritella communis* (30%), *Turbonilla* sp. (10%), *Loripes orbiculatus* (10%), and *Dendropoma* sp. (10%) dominating. Small brackish gastropods (*Hydrobia truncata*, *Bittium reticulatum* and *Cerithium vulgatum*) are also common (30%). *Turritella communis* is a marine suspension-feeding taxon living in shallow-marine and tidal-flat environments (Waite and Allmon 2013). *Loripes orbiculatus* is frequently associated with seagrasses such as *Zostera* and *Cymodocea* (Salem et al. 2014) but is also common in shallow intertidal and subtidal coastal waters. Facies Fb-c is also characterised by high percentages of miliolids (60%) and agglutinated taxa (*Miliammina* sp., *Agglutinella* sp., *Siphonaperta agglutinans*). In addition to molluscs and foraminifera, the transition from a terrestrial to an open embayment (around 6000 BCE, 7950 cal yr BP) is also indicated by fine-sand deposits that are enriched in marine elemental ratios (Fig. 18b). Sediments of this transgression overlie the azoic alluvial deposits and concur with the maximum sea level stand of the MIS-1 transgression (7000–6500 yr BP; Zazo et al. 1993; Sen and Banerjee 2016).

The transgression has also been recorded on the Skhira coast by Zaïbi et al. (2016; core TR1, 7460 cal yr BP) and at the Boujmel Lagoon (southeastern Tunisia, approximately 7500–8000 cal yr BP; Lakhdar et al. 2006). In contrast to the coast at Thyna, the northern coast of Sfax experienced strong uplift during the Holocene. The first marine transgression records north of Sfax are therefore delayed (dated to 4600 cal yr BP; Khadraoui et al. 2019).

Following the first transgression at around 6000 BCE, the environmental conditions shifted to a restricted lagoonal habitat between 6000 and 2500 BCE. In core TH1, facies Fd and Fe are distinguished from the lower facies by the progressive enrichment of lagoonal molluscs (up to 70%). This facies is characterised by *Cerithium vulgatum* (30%), *Hydrobia truncata* (20%) and *Bittium reticulatum* (20%) and by the disappearance of coastal species (*Natica* sp., *Gibbula umbilicalis*, *Nassarius sufflatus* and *Hexaplex trunculus*) in the upper part of Fe.

Facies Fd to Fe also record the disappearance of miliolids and rosalinids and the enrichment in ammoniids (80%), which are typical indicators of shallow, intertidal and stressed environmental conditions. Facies Fe, covering the interval between 3035 BCE (180 cm dbs) and 2591 BCE (140 cm dbs), also reveals a strong decrease in marine elemental ratios (Sr/Al, Ca/Al, Cl/Al, and S/Al). The enrichment of the fine fraction from 10% in Fd to 20% in Fe and the dominance of lagoonal foraminifera and mollusc taxa in Fd and Fe indicate a restricted, stressed intertidal environment favouring the abundance of stress-tolerant taxa (*Ammonia* spp.). The environmental transformation is also recorded by the absence of rosalinids and peneroplids in facies FI to FII of core TH4, where ammoniids constitute up

to 80% (in the interval 170–120 cm) and miliolids decrease and finally disappear. Facies F3 (core TH2), however, shows a dominance of elphidiids (30%) and miliolids (50%), indicating that an open embayment environment prevailed until at least 2394 BCE.

The differences recorded between the sediments of cores TH1, TH4 and TH2 are probably due to the formation of a sand spit that allowed a lagoon and salt marshes to form around the promontory, as documented on historical maps (Figs. 1D, 18c). As the lagoon had developed, the area was an ideal location for the construction of a small harbour. At about the same time (4130 and 6800 years BP), the nearby Boujmel lagoon developed, in which an organic-rich facies was deposited (Lakhdar et al. 2006). Based on pollen analyses, Jaouadi et al. (2015) reconstruct a grass steppe for the area of the Jeffar coastal plains and a typical Mediterranean scrub landscape in the mountainous hinterland. From the relatively thick lamellar gypsum layers of the Sebkhah El Melah, Aneur et al. (2021) reconstructed a rather hot and dry climatic period for the period between 5000 and 3200 BP.

Around 365 AD, all four cores show striking sedimentological features indicating drastic changes (Figs. 14, 15, 16). These changes are marked by the occurrence of bioclastic sands, changes in the preservation of biotas, and changes in geochemical proxies. In core TH1, the muddy sands (Ff, 22 cm) are rich in lithoclasts, with the coarse fraction (> 500 µm) reaching up to 30% and the fine fraction (< 63 µm) up to 25%. The sands contain abundant fragmented shells of marine and brackish species (50% of the total fraction > 500 µm), intact lagoonal molluscs, and increasing abundances of the brackish gastropod *Hydrobia truncata* (30%) and the white furrow bivalve *Abra alba* (40%). In addition, coastal gastropods such as *Natica* sp. (2%), *Hexaplex trunculus* (2%) and *Gibbula umbilicalis* (2%) reappear together with articulated valves of *Cerastoderma glaucum* and *Ruditapes decussatus*. In general, the mollusc shells are frequently bioeroded. Compared to other facies, this horizon is more diverse, has more species and shows the highest number of individuals (100 ind./gr).

The foraminiferal fauna observed in this peculiar facies (Ff) is dominated by ammoniids (80%), with most of the tests broken or damaged. Among the ostracods recorded, the brackish species *Cyprideis torosa* is the most abundant. The preservation of ostracod valves is generally poor (pyritised/secondary calcification), which suggests that chemical, physical and out-of-habitat transport processes were involved (Ben Hamad et al. 2018; Frenzel and Boomer 2005; Keatings et al. 2007).

Analyses of marine elemental ratios in facies Ff (core TH1) and F4 (core TH2) show strong increases in Ca/Al and Sr/Al, and reductions in detrital element ratios (Si/Al and Zr/Al) are recorded in Ff (TH1 core) and F4 (TH2 core).

Taken together, the palaeontological, sedimentological and geochemical analyses indicate fundamentally different depositional conditions, which may be attributable to a high-energy event (see also Dawson 1994; Dawson and Stewart 2007; Engel et al. 2016; Khadraoui et al. 2019). The high-energy event most probably occurred in the interval between 396 BCE and 325 CE, as indicated by the radiocarbon ages obtained from sediment of Fe (2591 BCE) and Fi (325 CE) in core TH1 and FDa (396 BCE) and FF (1635 CE) in core TH5 (Table 2).

Facies Fg in core TH1 is composed of muddy sand that is rich in bioclasts and reveals a reduction in the coarse fraction. This facies contains rare peneroplid and rosalinid foraminifera and shows reductions in marine element ratios (Ca/Al and Sr/Al). Facies Fh, in turn, differs from facies Fg by an abrupt increase in the coarse fraction (60%) and by its richness in mega-pottery fragments, large lithoclasts, abundant charcoal particles, plant seeds (olive pits and grape seeds) and varnished wood fragments (Fig. 7B, Fh). Brackish foraminifera and lagoonal molluscs increase in this facies, but foraminiferal tests and mollusc shells are mostly broken, as recorded in facies Ff. The dominance of ammoniid foraminifera (up to 90%) and the reduction in the ratio of marine elements suggest that freshwater input had an influence on faunal composition, shell preservation and depositional conditions.

Historical documents show that Thyna underwent a profound transformation of its urban landscape in late antiquity (Servonnet and Lafitte 1888). The city expanded until the middle of the third century CE, after which it declined for almost a century and only experienced a renaissance again in the fourth century CE (Thirion 1957; Fendri 1985). Thirion (1957) reports that painted fragments of earlier buildings from the third century have been found in the western part of the city. The archaeological finds from Thyna also point to a destructive high-energy event at around 365 CE. These document the destruction of the Thyna thermal complex located 50 m north of the shore (Thirion 1957), the retrofitting of a double-walled retaining wall (Fig. 7A–C; Thirion 1957; Fendri 1964) and the construction times of the walls (Fig. 7D). The destruction of Thyna coincides with the earthquake and the resulting tsunami in Crete (365 CE). Whether and in what form this high-energy event affected the city of Thyna and whether a tsunami was actually responsible for the partial destruction of the city and harbour cannot be conclusively answered here. However, faunal shifts, geochemical proxies and sedimentary changes documented and dated here point to a high-energy event that has also been previously documented in outcrops north of Sfax (Khadraoui et al. 2019) and along the Acholla coast (Bahrouni et al. 2021; Kamoun et al. 2021).

After the high-energy event, there is evidence from the sediments of all drill cores that a partially open lagoon, protected by a sand barrier, was again in place off the coast. In fact, facies Fi (core TH1), FV (core TH4) and F5 (core TH2) show an increase in ammoniid taxa, reductions in elphidiids, miliolids and peneroplids, and an impoverishment of foraminiferal diversity. The dominance of the fine fraction (<63 µm) in these facies also supports this scenario. Later, the Romans rebuilt the destroyed parts of the city and harbour and erected a wall to protect the city from extreme events (Fig. 18e).

After the open lagoon formed off the coast of Thyna, the sediments and composition of the marine fauna changed. This is shown by an increase in foraminifera in the upper layers of cores TH1 and TH4. The brown clays (Fj) and red silts (Fk) of core TH1 record the reappearance (from 30 to 5 cm dbs) of miliolids (50–80%), peneroplids (2.5–2.5%) and rosalinids (2–5%), and the number of individuals is highest in this core (870–2000 ind./gr) (Fig. 19). Many shells and peneroplid tests are broken. High marine-element ratios (Cl/Al, Sr/Al, S/Al and Ca/Al) are also characteristic of this interval. The FV facies (core TH4) also shows a reappearance of foraminifera from 20 to 2.5 cm dbs with an enrichment of miliolids (70–90%), peneroplids (3–5%) and rosalinids (3–5%) and an increase in the number of specimens (280–850 ind./gr) (Fig. 20). *Hauerina* sp. and *Peneroplis planatus* are the dominant taxa. The proxies recorded in facies Fj–Fk (core TH1) and FV (core TH4) are complementary and thus allow the reconstruction of the palaeoenvironment of the Thyna coast. Indications of an increase in marine influence and further opening of the lagoon in the nineteenth and twentieth centuries can also be seen in the enrichment of miliolids, the increases in marine element ratios, and the decrease in ammoniid foraminifera.

Our interpretation is consistent with archaeological and geological studies, which provide evidence that rising sea levels had a significant impact on coastal areas in historical times. At the city of Acholla, the Roman pier has been under water since the fifth century AD (Kamoun et al. 2021), and the Roman pier at Thapsus is now under water—about 2 m below the present sea level (Slim et al. 2004; Kamoun et al. 2022). Flooding of the Kerkennah coast due to a sea level rise of the order of 2 m since antiquity is also mentioned by Burolet (1979) and Slim et al. (2004). In addition, a rapid rise in relative mean sea level was recorded at the Sfax tide gauge between 1910 and 1856 (5.7 mm per year; Pirazzoli 1986). This rate is four times higher than the absolute global sea level rise, indicating that this coastal section is subject to not only sea level fluctuations but also to subsidence.

The environmental evolution scenario illustrated in Fig. 18 is also supported by statistical analysis (the elbow method), which delineates four faunal groups along the core. The four faunal groups identified are consistent with a scenario that involves a first marine transgression, the development of a lagoon, a high-energy event and a second marine transgression.

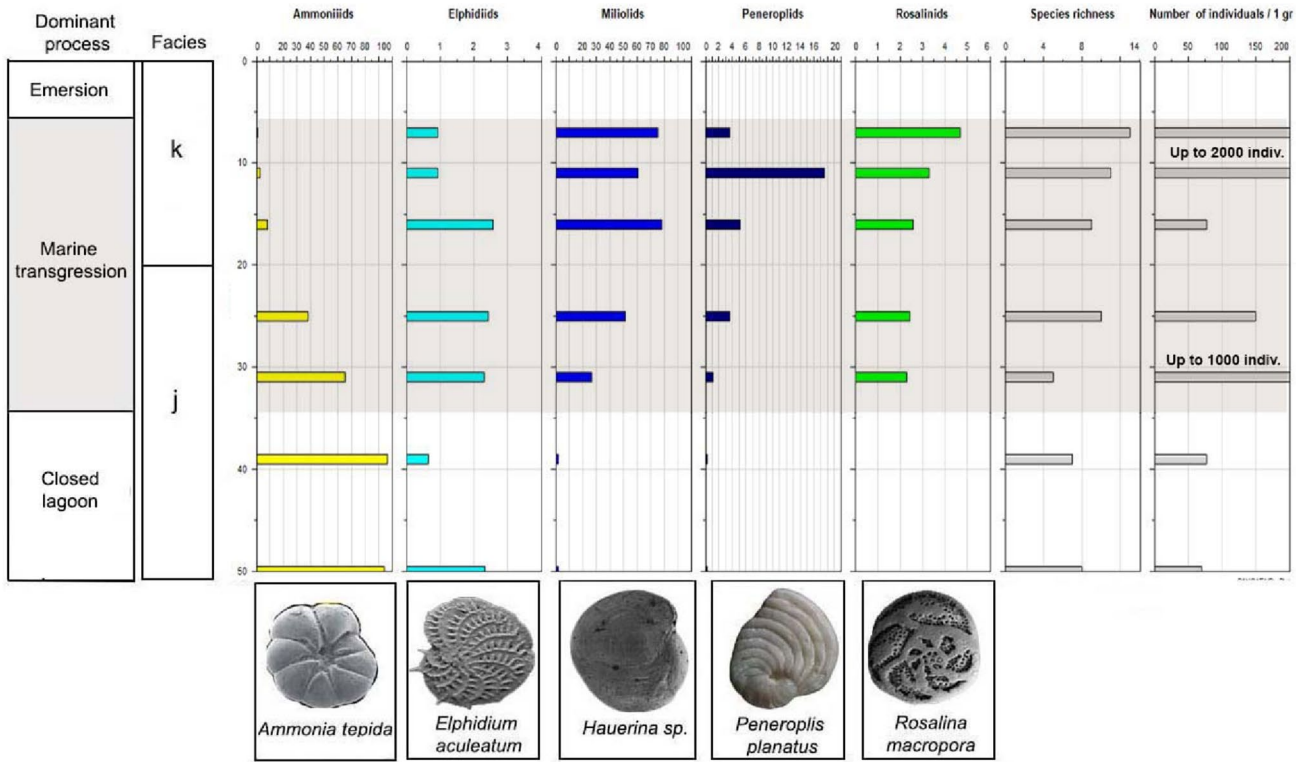


Fig. 19 Abundances of individual groups of foraminifera in the facies Fj and Fk in core TH1. Species richness and abundances (number of individuals/gr), interpreted environments, and SEM illustrations of dominant species of foraminifera

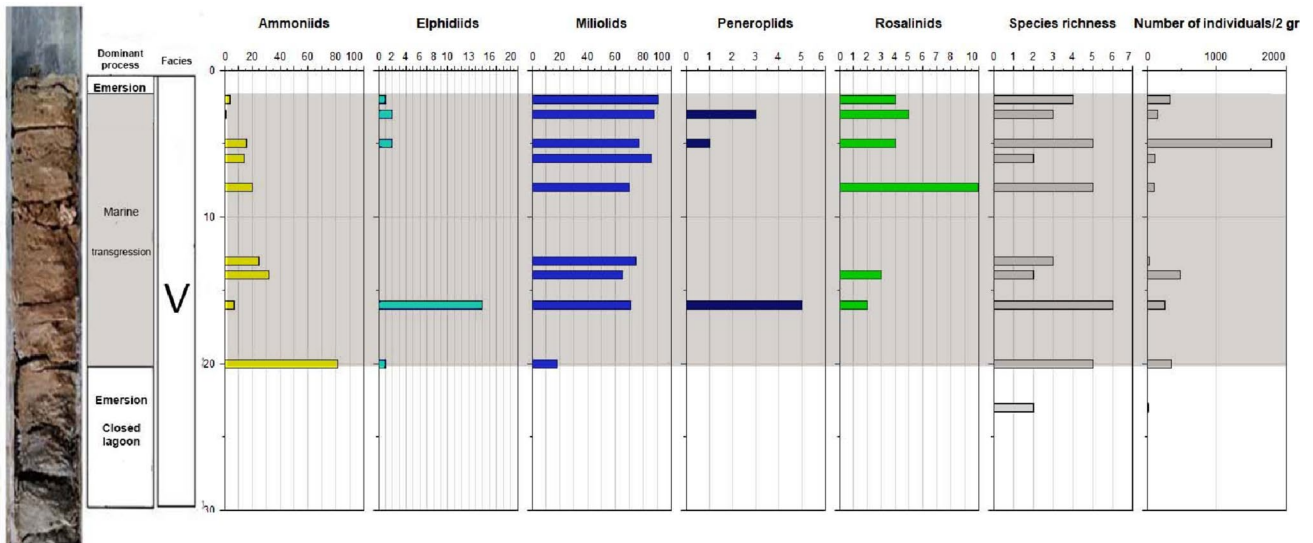


Fig. 20 Main foraminifera ecologic group species of the facies FV of core TH4. Species richness and abundances (number of individuals/2 gr) and interpreted environments

### Conclusions

This study used multiproxy analyses of sediment cores to reconstruct the coastal evolution of Thyna. Our results show

that after the sea level rise in the Upper Pleistocene and Lower Holocene, an open lagoon developed over a former alluvial plain. This lagoon development can be dated to the period between 6234–5733 BCE to 2874–2352 BCE.



The open lagoon was gradually enclosed, as evidenced by a decrease in grain size and a decline in miliolids and elphidiids combined with a dominance of ammoniids. In the fourth century, and most likely in the year 365 AD, the lagoon and the historic city of Thyna were hit by a high-energy storm event, which is reflected in the deposition of bioclastic sands. The deposits of this event show the typical characteristics of a high-energy impact (a basal erosional surface, rip-up clasts, the remains of a mixture of marine and brackish mollusc shells, assemblages of damaged and broken foraminiferal tests, transported molluscs, pottery fragments, and charcoal particles). This extreme event is possibly responsible for the partial destruction of the Roman city of Thyna. The destruction of Thyna coincides with the earthquake and the resulting tsunami on Crete (365 AD) and coincides with previous investigations into the impact of a tsunami on the coast of Tunisia. However, further investigations are necessary to conclusively confirm this event for Thyna as well. After the high-energy event, a partially open lagoon developed again off the coast, protected from the open sea by a sand barrier. Over the last few centuries, a greater marine influence has become apparent in the partly open Thyna lagoon, caused on the one hand by the current sea level rise but presumably also by the subsidence of the coastal region off Thyna.

**Funding** This work was carried out with the financial support of the Tunisian–Portuguese bilateral cooperation project “Vulnerability of wetlands, impact of pollution, climate change and extreme events”, funded by both the Tunisian Ministry of Higher Education and Scientific Research and the Portuguese Fundação para a Ciência e Tecnologia, 2019/2022 (University of Sfax, Faculty of Sciences, University of Lisbon). This work was also funded by the Portuguese Fundação para a Ciência e a Tecnologia (FCT) I.P./MCTES through national funds (PIDDAC)—UIDB/50019/2020—<https://doi.org/10.54499/UIDB/50019/2020>, UIDP/50019/2020 (<https://doi.org/10.54499/UIDP/50019/2020>) and LA/P/0068/2020 (<https://doi.org/10.54499/LA/P/0068/2020>). MK also benefitted from a research stay at the micropalaeontology laboratory at the University of Bonn.

## Declarations

**Conflict of interest** The authors have no conflicts of interest to declare that are relevant to the content of this article.

## References

- Amari A (1984) Contribution à la connaissance hydrologique et sédimentologique de la plate forme des Kerkennah. Thèse de 3ème cycle. Géol Appliquée au Domaine Marin et Océanologie. Fac. Sci. Tunis, Tunis, pp 1–251
- Ameur MB, Masmoudi S, Yaich C (2021) Flood and sandstorm events recorded in holocene sebkha deposits in Southeastern Tunisia: evidence from magnetic and geochemical properties. *Quatern Int* 571:46–57
- Bahrouni N, Meghraoui M, Başak Bayraktar H, Lorito S, Zagrarri MF, Bel Mabrouk N (2021) Evidence of tsunami deposits in East Tunisia coastline contemporaneous of the AD 365 Crete earthquake: field data and modelling. EGU General Assembly 2021, online, 19–30 Apr 2021, EGU21-9104. <https://doi.org/10.5194/egusphere-egu21-9104>
- Barill-Boyer AL, Barillé L, Massé H, Razet D, Heral M (2003) Correction for particulate organic matter as estimated by loss on ignition in estuarine ecosystems. *Estuar Coast Shelf Sci* 58:147–153. [https://doi.org/10.1016/S0272-7714\(03\)00069-6](https://doi.org/10.1016/S0272-7714(03)00069-6)
- Basquin E, El Baz A, Sainte-Marie J, Rabaute A, Thomas M, Lafuerza S, Creach A (2023) Evaluation of tsunami inundation in the plain of Martil (north Morocco): comparison of four inundation estimation methods. *Nat Hazards Res* 3:494–507
- Ben Hamad A, Viehberg FA, Khadraoui A, Zaïbi C, Trabelsi Y, Mouanga GH, Langer MR, Abida H, Kamoun F (2018) Water level and atmospheric humidity history of Lake Ichkeul (northern Tunisia) during the last 3000 years. *Arab J Geosci* 11:1–19
- Ben Khalifa K, Zaïbi C, Bonnin J, Carbonel P, Zouari K, Mnif T, Kamoun F (2019) Holocene environment changes in the Hachichina wetland (Gulf of Gabes, Tunisia) evidenced by foraminifera and ostracods, geochemical proxies and sedimentological analysis. *Riv Ital Paleontol S* 125:517–549
- Benzécri JP (1980) *Pratique de l'analyse des données*. Éditions Dunod, Paris
- Beuria PC, Biswal SK, Mishra BK, Roy GG (2017) Study on kinetics of thermal decomposition of low LOI goethetic hematite iron ore. *Int J Min Sci Technol* 27(6):1031–1036
- Blott S, Kenneth P (2000) A grain size distribution and statistics package for the analysis of unconsolidated sediments by sieving or by laser granulometer. *Grandstat. Earth Surf Proc Land* 26:1237–1248. <https://doi.org/10.1002/esp.261>
- Bony G, Marriner N, Morhange C, Kaniewski D, Perinçek D (2012) A high-energy deposit in the Byzantine harbour of Yenikapi, Istanbul (Turkey). *Quatern Int* 266:117–130
- Bouaziz S, Sgari A, Ben Akacha M (2004) Geological map of Agreb. Office National des Mines, Tunis
- Bouchet P, Rocroi JP (2005) Nomenclator of bivalve families with a classification of bivalve families malacologia. *Inst Malacol* 5:21–184
- Brogan L, Kenyon K (1966) Cambridge expedition to Sabratha 1966. Royal Geographical Society, London
- Burollet PF (1979) La mer Pélagienne, les apports de l'archéologie. *Géol Méditerran* 6(1):309–313
- Calvert SE, Pedersen TF (2007) Chapter fourteen elemental proxies for palaeoclimatic and palaeoceanographic variability in marine sediments: interpretation and application. *Dev Mar Geol* 1:567–644
- Chagué-Goff C, Dawson S, Goff JR, Zachariassen J, Berryman KR, Garnett D, Mildenhall DC (2002) A tsunami (ca. 6300 years BP) and other Holocene environmental changes, northern Hawke's Bay, New Zealand. *Sediment Geol* 150(1–2):89–102
- Chagué-Goff C, Andrew A, Szczuciński W, Goff J, Nishimura Y (2012) Geochemical signatures up to the maximum inundation of the 2011 Tohoku-oki tsunami—implications for the 869 AD Jogan and other palaeotsunamis. *Sed Geol* 282:65–77
- Cimerman F, Langer MR (1991) Mediterranean Foraminifera. *Slovenska Akademija Znanosti, Ljubljana*, p 118
- Damak M, Ismail MB, Fourati R, Elleuch B, Kallel M (2019) Survey: sources, distribution and effects of marine pollution in the Monastir Bay (eastern of Tunisia, Central Mediterranean Sea). *Saudi J Life Sci*. <https://doi.org/10.1276/haya.2019.4.5.5>
- Dankers N, Laane R (1983) A comparison of wet oxidation and loss on ignition of organic material in suspended matter. *Environ Technol Lett* 4:283–290. <https://doi.org/10.1080/09593338309384208>

- Dawson AG (1994) Geomorphological effects of tsunami run-up and backwash. *Geomorphology* 10:83–94
- Dawson S (2007) Diatom biostratigraphy of tsunami deposits: examples from the 1998 Papua New Guinea tsunami. *Sed Geol* 200:328–335
- Dawson AG, Shi S (2000) Tsunami deposits. *Pure Appl Geophys* 157:875–897
- Dawson AG, Stewart I (2007) Tsunami deposits in the geological record. *Sed Geol* 200(3–4):166–183
- De Martini PM, Graziani L, Maramai A, Orefice S, Pantosti D, Smedile A (2020) Tsunamis in the Mediterranean sea. Reference module in earth systems and environmental sciences. Elsevier, Amsterdam
- Dura T, Hemphill-Haley E (2020) Diatoms in tsunami deposits. Geological records of tsunamis and other extreme waves. Elsevier, Amsterdam, pp 291–322
- Dweck J (2008) Qualitative and quantitative characterization of Brazilian natural and organophilic clays by thermal analysis. *J Therm Anal Calorim* 92(1):129–135
- El Kateb A, Stalder C, Rüggeberg A, Neururer C, Spangenberg JE, Spezzaferri S (2018) Impact of industrial phosphate waste discharge on the marine environment in the Gulf of Gabes (Tunisia). *PLoS One* 13(5):0197731
- Engel M, Oetjen J, May SM, Brückner H (2016) Tsunami deposits of the Caribbean—towards an improved coastal hazard assessment. *Earth Sci Rev* 163:260–296
- Fajemila OT, Langer MR, Lipps JH (2015) Spatial patterns in the distribution, diversity and abundance of benthic foraminifera around Moorea (Society Archipelago, French Polynesia). *PLoS ONE* 10(12):e0145752. <https://doi.org/10.1371/journal.pone.0145752>
- Fantar M, Spanu PG, Zucc R (2019) Un decennio di esplorazioni nella colonia Iulia Neapolis in Africa Proconsolare. *Atti dell'Accademia Nazionale dei Lincei, Anno CDXV, Rendiconti Serie IX, Volume XXIX, Fascicolo 3–4*:381–419
- Fendri M (1964) Les thermes des mois de Thina. *Les Cahiers Tunis* 12(45–46):47–67
- Fendri M (1985) Cités antiques et villas romaines de la région sfaxienne. *Africa* 9:151–208
- Fischer P, Finkler C, Röbbke BR, Baika K, Hadler H, Willershäuser T, Vött A (2016) Impact of Holocene tsunamis detected in lagoonal environments on Corfu (Ionian Islands, Greece): geomorphological, sedimentary and microfaunal evidence. *Quatern Int* 401:4–16
- Flemming BW (2000) A revised textural classification of gravel-free muddy sediments on the basis of ternary diagrams. *Cont Shelf Res* 20(10–11):1125–1137
- Folk RL, Ward WC (1957) Brazos River bar [Texas]; a study in the significance of grain size parameters. *J Sediment Res* 27(1):3–26
- Frébourg G, Hasler CA, Davaud E (2010) Catastrophic event recorded among Holocene eolianites (Sidi Salem Formation, SE Tunisia). *Sediment Geol* 224:38–48
- Freitas MDC, Andrade C, Cruces A (2002) The geological record of environmental changes in southwestern Portuguese coastal lagoons since the Lateglacial. *Quatern Int* 93:161–170
- Frenzel P, Boomer I (2005) The use of ostracods from marginal marine, brackish waters as bioindicators of modern and quaternary environmental change. *Palaeogeogr Palaeoclimatol Palaeoecol* 225:68–92
- Gargouri D, Moez B, Azri C (2015) Sediment quality and potential toxicity assessment in two open/semiclosed Mediterranean sea areas: a case study of Sfax Coast (Tunisia). *Water Environ Res* 87(5):470–479
- Gastaldi G, Licinus, FE (1564) The drawing of the modern geography of the Whole Africa. Retrieved from the Library of Congress. <https://www.loc.gov/item/2021668433/>
- Ghribi R, Sghari A, Bouaziz S (2006) Le bassin de l'oued Ouadrane (Tunisie méridionale): évolution géomorphologique et néotectonique. *Notes Serv Géol Tunisie* 74:77–97
- Goff J, Chagué-Goff C (2015) Three large tsunamis on the non-subduction, western side of New Zealand over the past 700 years. *Rev Mar Geol* 363:243–260
- Govin A, Holzwarth U, Heslop D, Ford Keeling L, Zabel M, Mulitza S, Chiessi CM (2012) Distribution of major elements in Atlantic surface sediments (36 N–49 S): imprint of terrigenous input and continental weathering. *Geochem Geophys Geosyst.* <https://doi.org/10.1029/2011GC003785>
- Guidoboni E, Comastri A, Giusto Traina G (1994) Catalogue of ancient earthquakes in the Mediterranean area up to the 10th century. Istituto Nazionale di Geofisica, Rome, p 486
- Hammer Ø, Harper DA, Ryan PD (2001) PAST: Paleontological statistics software package for education and data analysis. *Palaeontol Electr* 4:9
- Hartigan JA, Wong MA (1979) Algorithm AS 136: a k-means clustering algorithm. *Roy Stat Soc Ser C (Appl Stat)* 28:100–108
- Hawkes AD (2020) Foraminifera in tsunami deposits. Geological records of tsunamis and other extreme waves. Elsevier, Amsterdam, pp 239–259
- Hawkes AD, Bird M, Cowie S, Grundy-Warr C, Horton BP, ShauHwai AT, Law L, Macgregor C, Nott J, Ong JE, Rigg J, Robinson R, Tan-Mullins M, Sa TT, Yasin Z, Aik LW (2007) Sediments deposited by the 2004 Indian Ocean Tsunami along the Malaysia–Thailand Peninsula. *Mar Geol* 242:169–190
- Heaton TJ, Köhler P, Butzin M, Bard E, Reimer RW, Austin W, Ramsey CB, Grootes PM, Hughen KA, Kromer B, Adkins J, Burke A, Cook MS, Olsen J, Skinner LC (2020) Marine20—the marine radiocarbon age calibration curve (0–55,000 cal BP). *Radiocarbon* 62(4):779–820. <https://doi.org/10.1017/RDC.2020.68>
- Hussain SM, Mohan SP, Jonathan MP (2010) Ostracoda as an aid in identifying 2004 tsunami sediments: a report from SE coast of India. *Nat Hazards* 55:513–522
- Jaffe BE, Goto K, Sugawara D, Richmond BM, Fujino S, Nishimura Y (2012) Flow speed estimated by inverse modeling of sandy tsunami deposits: results from the 11 March 2011 tsunami on the coastal plain near the Sendai Airport, Honshu, Japan. *Sed Geol* 282:90–109
- Jaouadi S, Lebreton V, Mannai-Tayech B, Lakhdar R, Soussi M (2015) Apport de l'analyse pollinique des sédiments de la sebkha Boujmel (Sud-Est tunisien) à la reconstitution des paléopaysages et paléoclimats holocènes en milieu aride. *Méditerranée* 125:39–49
- Judd K, Chagué-Goff C, Goff J, Gadd P, Zawadzki A, Fierro D (2017) Multi-proxy evidence for small historical tsunamis leaving little or no sedimentary record. *Mar Geol* 385:204–215
- Kamoun M, Zaïbi C, Langer MR, Carbonel P, Ben Youssef M (2021) Coastal dynamics and the evolution of the Acholla lagoon (Gulf of Gabes, Tunisia): a multiproxy approach. *Arab J Geosci* 14:1–26
- Kamoun M, Langer MR, Zaïbi C, Ben Youssef M (2022) Meghalayan environmental evolution of the Thapsus coast (Tunisia) as inferred from sedimentological and micropaleontological proxies. *J Micropalaeontol* 41(2):129–147
- Keatings KW, Hawkes I, Holmes JA, Flower RJ, Leng MJ, Abu-Zied RH, Lord AR (2007) Evaluation of ostracod-based palaeoenvironmental reconstruction with instrumental data from the arid Faiyum depression. *Egypt J Paleolimnol* 38:261–283
- Kelletat D, Schellmann G (2002) Tsunamis on Cyprus—field evidences and 14C dating results. *Z Geomorphol* 46:19–34
- Kelletat D, Whelan F, Bartel P, Scheffers A (2005) New tsunami evidences in Southern Spain—Cabo de Trafalgar and Mallorca

- Island. In: Sanjaume E, Matheu JF (eds) *Geomorfologia Litoral I Quaternari: Homenatge al professor Vincenç M. Rosselló I Verger*. Universitat de València, València, pp 215–222
- Khadraoui A, Kamoun M, Hamad AB, Zaïbi C, Bonnin J, Viehberg F, Kamoun F (2018) New insights from microfauna associations characterizing palaeoenvironments, sea level fluctuations and a tsunami event along Sfax Northern coast (Gulf of Gabes, Tunisia) during the Late Pleistocene-Holocene. *J Afr Earth Sci* 147:411–429
- Khadraoui A, Zaïbi C, Carbonel P, Bonnin J, Kamoun F (2019) Ostracods and mollusks in northern Sfax coast: reconstruction of Holocene paleoenvironmental changes and associated forcing. *Geo-Mar Lett* 39:313–336
- Kitamura A, Ito M, Ikuta R, Ikeda M (2018) Using molluscan assemblages from paleotsunami deposits to evaluate the influence of topography on the magnitude of late Holocene mega-tsunamis on Ishigaki Island, Japan. *Prog Earth Planet Sci* 5(1):1–10
- Kohila BS, Dezileau L, Boussetta S, Melki T, Kallel N (2021) Extreme marine events revealed by lagoonal sedimentary records in Ghar El Melh during the last 2500 years in the northeast of Tunisia. *Nat Hazard* 21(12):3645–3661
- Kortekaas S (2002) *Tsunamis, storms and earthquakes: distinguishing coastal flooding events*. Doctoral dissertation. Coventry University, Coventry
- Kortekaas S, Dawson A (2007) Distinguishing tsunami and storm deposits: an example from Martinhal, SW Portugal. *Sediment Geol* 200:208–221
- Kortekaas S, Papadopoulos GA, Ganas A, Diakantoni A (2003) Geological identification of historical tsunamis in the Gulf of Corinth, Greece. *Geophys Res Abstr* 5(09909)
- Lakhdar R, Soussi M, Ben ismail MH, M'rabet A (2006) A Mediterranean Holocene restricted coastal lagoon under arid climate: case of the sedimentary record of the Sabkha Boujmel (SE Tunisia). *Palaeogeogr Palaeoclimatol Palaeoecol* 241:177–191
- Langer MR (1988) Recent epiphytic foraminifera from vulcano (Mediterranean Sea). *Rev Paléobiol* 86:827–832
- Langer MR (1993) Epiphytic foraminifera. *Mar Micropal* 20:235–265. <https://doi.org/10.1016/0377-8398>
- Langer MR, Schmidt-Sinns J (2006) The 100 most common Foraminifera from the Bay of Fetovaia, Elba Island (Mediterranean Sea). *Institut für Paläontologie, Universität Bonn, Bonn*, pp 1–37
- Mamo B, Strotz L, Dominey-Howes D (2009) Tsunami sediments and their foraminiferal assemblages. *Earth Sci Rev* 96:263–278
- Martinez-Ruiz F, Kastner M, Gallego-Torres D, Rodrigo-Gámiz M, Nieto-Moreno V, Ortega-Huertas M (2015) Paleoclimatic and paleoceanographic over the past 20,000 yr in the Mediterranean Sea Basins as indicated by sediment elemental proxies. *Quatern Sci Rev* 107:25–46
- Mastroruzzi G, Sansò P (2004) Large boulder accumulations by extreme waves along the Adriatic coast of southern Apulia (Italy). *Quatern Int* 120(1):173–184
- May SM, Willershäuser T, Vött A (2010) Boulder transport by high-energy wave events at Cap Bon (NE Tunisia). *Coastline Rep* 16:1–10
- Mook DH, Hoskin CM (1982) Organic determinations by ignition: caution advised. *Estuar Coast Shelf Sci* 15:697–699. [https://doi.org/10.1016/0272-7714\(82\)90080-4](https://doi.org/10.1016/0272-7714(82)90080-4)
- Moreira S, Costa PJM, Andrade C, Lira CP, Freitas MC, Oliveira MA, Reichart G-J (2017) High resolution geochemical and grain-size analysis of the AD 1755 tsunami deposit: insights into the inland extent and inundation phases. *Mar Geol* 390:94–105. <https://doi.org/10.1016/j.margeo.2017.04.007>
- Morton RA, Gelfenbaum G, Jaffe BE (2007) Physical criteria for distinguishing sandy tsunami and storm deposits using modern examples. *Sediment Geol* 200:184–207
- Morton RA, Richmond BM, Jaffe BE, Gelfenbaum G (2008) Coarse-clast ridge complexes of the Caribbean: a preliminary basis for distinguishing tsunami and storm-wave origins. *J Sediment Res* 78(9):624–637
- Nagendra R, Kannan BK, Sajith C, Sen G, Reddy AN, Srinivasulu S (2005) A record of foraminiferal assemblage in tsunami sediments along Nagappattinam coast, Tamil Nadu. *Curr Sci* 89(11):1947–1952
- Oueslati A (2021) Sur l'érosion marine des vestiges archéologiques antiques du littoral tunisien et les risques d'une accélération de leur dégradation. *Méditerran Rev Géogr Pays Méditerran* 133:97–106
- Papadopoulos GA (2009) Chapter 17: Tsunamis. In: Woodward J (ed) *Physical geography of the Mediterranean*. Oxford University Press, Oxford, pp 493–512
- Picard J (1900) *Les travaux publics du protectorat français en Tunisie*. Mines, service topographique, navigation et pêches maritimes. Direction générale des travaux publics, Tunis
- Pilarczyk JE, Dura T, Horton BP, Engelhart SE, Kemp AC, Sawai Y (2014) Microfossils from coastal environments as indicators of paleo-earthquakes, tsunamis and storms. *Palaeogeogr Palaeoclimatol Palaeoecol* 413:144–157
- Pilarczyk JE, Sawai Y, Matsumoto D, Namegaya Y, Nishida N, Ikehara K, Horton BP (2020) Constraining sediment provenance for tsunami deposits using distributions of grain size and foraminifera from the Kujukuri coastline and shelf, Japan. *Sedimentology* 67(3):1373–1392
- Pirazzoli PA (1986) Secular trends of relative sea-level (RSL) changes indicated by tide-gauge records. *J Coast Res (Spec Issue)* 1:1–26
- Polonia A, Bonatti E, Camerlenghi A, Lucchi RG, Panieri G, Gasperini L (2013) Mediterranean megaturbidite triggered by the AD 365 Crete earthquake and tsunami. *Sci Rep* 3(1):1285
- Puga-Bernabéu Á, Aguirre J (2017) Contrasting storm-versus tsunami-related shell beds in shallow-water ramps. *Palaeogeogr Palaeoclimatol Palaeoecol* 471:1–14
- Putra PS, Aswan A, Maryunani KA, Yulianto E, Kongko W (2019) Field survey of the 2018 Sulawesi tsunami deposits. *Pure Appl Geophys* 176:2203–2213
- Putra PS, Yulianto E, Nugroho SH (2022) Distribution patterns of foraminifera in paleotsunami layers: a review. *Nat Hazards Res* 3:1–13
- Quintela M, Costa PJM, Fatela F, Drago T, Hoska N, Andrade C, Freitas MC (2016) The AD 1755 tsunami deposits onshore and offshore of Algarve (south Portugal): sediment transport interpretations based on the study of foraminifera assemblages. *Quatern Int* 408:123–138
- Reimer PJ, Austin WE, Bard E, Bayliss A, Blackwell PG, Ramsey CB, Talamo S (2020) The IntCal20 Northern Hemisphere radiocarbon age calibration curve (0–55 cal kBP). *Radiocarbon* 62(4):725–757
- Rethemeyer J, Gierga HS, Stolz A, Wotte A, Wischhöfer P, Dewald A (2019) Current sample preparation and analytical capabilities of the radiocarbon laboratory at Cologne AMS. *Radiocarbon* 61(5):1449–1460
- Ruiz F, Abad M, Cáceres LM, Vidal JR, Carretero MI, Pozo M, González-Regalado ML (2010) Ostracods as tsunami tracers in Holocene sequences. *Quatern Res* 73:130–135
- Salama A, Meghraoui M, El Gabry M, Maoche S, Hussein MH, Korrat I (2018) Paleotsunami deposits along the coast of Egypt correlate with historical earthquake records of eastern Mediterranean. *Nat Hazard* 18(8):2203–2219
- Salem MVA, Van Der Geest M, Piersma T, Saoud Y, Van Gils JA (2014) Seasonal changes in mollusc abundance in a tropical intertidal ecosystem, Banc d'Arguin (Mauritania): testing the 'depletion by shorebirds' hypothesis. *Estuar Coast Shelf Sci* 136:26–34

- Scheffers A, Scheffers SR (2007) Tsunami deposits on the coastline of West Crete (Greece). *Earth Planet Sci Lett* 259:613–624
- Sen PK, Banerjee M (2016) Holocene biostratigraphic zones corresponding litho-chronostratigraphy, environment of deposition and successive changes in the geomorphology of Bengal Basin, India during last 10,000 years. *Int J Geosci* 7(4):615–629
- Servonnet J, Lafitte F (1888) *En Tunisie. Le Golfe de Gabès en 1888: Avec une lettre-préface de Jurien de la Gravière (4 cartes and 12 planches)*. Paris, Librairie algérienne, maritime et coloniale. Challamel et Cie Editeurs, Paris
- Slim H, Troussat P, Paskoff R, Oueslati A, Bonifay M, Lenne J (2004) *Le littoral de la Tunisie: Etude géoarchéologique et historique*. Éditions du Centre National de la Recherche Scientifique, Paris, pp 3–308
- Strezov V, Ziolkowski A, Evans TJ, Nelson PF (2010) Assessment of evolution of loss on ignition matter during heating of iron ores. *J Therm Anal Calorim* 100:901–907. <https://doi.org/10.1007/s10973-009-0398-4>
- Szczuciński W, Kokociński M, Rzeszewski M, Chagué-Goff C, Cachão M, Goto K, Sugawara D (2012) Sediment sources and sedimentation processes of 2011 Tohoku-oki tsunami deposits on the Sendai Plain, Japan—insights from diatoms, nannoliths and grain size distribution. *Sed Geol* 282:40–56
- Thirion J (1957) Un ensemble thermal avec mosaïque à Thina. *MEFRA* 1957:207–245
- Trog C, Höfer D, Frenzel P, Camacho S, Schneider H, Mäusbacher R (2013) A multi-proxy reconstruction and comparison of Holocene palaeoenvironmental changes in the Alvor and Alcantarilha estuaries (southern Portugal). *Rev Micropaléontol* 56(4):131–158
- Trubin YS, Kamoun M, Langer MR (2023) Environmental signatures preserved in extremely shallow-water benthic foraminifera assemblages from Oman, Arabian Sea. *J Foramin Res* 53(4):362–377
- Vigliotti L, Andrade C, Freitas MC, Capotondi L, Gallerani A, Bellucci LG (2019) Paleomagnetic, rock magnetic and geochemical study of the 1755 tsunami deposit at Boca do Rio (Algarve, Portugal). *Palaeogeogr Palaeoclimatol Palaeoecol* 514:550–566
- Waite R, Allmon WD (2013) Observations on the biology and sclerochronology of *Turritella leucostoma* (Valenciennes, 1832; Cerithioidea: Turritellidae) from the Gulf of California. *Am Malacol Bull* 31(2):297–310
- Wedepohl KH (1971) Environmental influences on the chemical composition of shales and clays. *Phys Chem Earth* 8:305–333
- Zaïbi C, Carbonel P, Kamoun F, Azri C, Kharroubi A, Kallel N, Fontugne M (2011) Évolution du trait de côte à l'Holocène supérieur dans la Sebkha El-Guettiate de Skhira (Golfe de Gabès, Tunisie) à travers sa faune d'ostracodes et de foraminifères. *Geobios* 44(1):101–115
- Zaïbi C, Kamoun F, Viehberg F, Carbonel P, Jedoui Y, Abida A, Fontugne M (2016) Impact of relative sea level and extreme climate events on the Southern Skhira coastline (Gulf of Gabes, Tunisia) during Holocene times: Ostracodes and foraminifera associations' response. *J Afr Earth Sci* 118:120–136
- Zazo C, Goy JL, Dabrio CJ, Bardaj T, Somoza L, Silva PG (1993) The last interglacial in the Mediterranean as a model for the present interglacial. *Glob Planet Change* 7:109–117

Springer Nature or its licensor (e.g. a society or other partner) holds exclusive rights to this article under a publishing agreement with the author(s) or other rightsholder(s); author self-archiving of the accepted manuscript version of this article is solely governed by the terms of such publishing agreement and applicable law.